



Derivation and simulation of a two-phase fluid deformable surface model

Elena Bachini^{1,‡}, Veit Krause¹, Ingo Nitschke¹ and Axel Voigt^{1,2,3,†}

¹Institute of Scientific Computing, TU Dresden, Germany

²Center for System Biology Dresden, Germany

³Cluster of Excellence, Physics of Life, TU Dresden, Germany

(Received 20 May 2023; revised 13 October 2023; accepted 1 November 2023)

To explore the impact of surface viscosity on coexisting fluid domains in biomembranes we consider two-phase fluid deformable surfaces as model systems for biomembranes. Such surfaces are modelled by incompressible surface Navier–Stokes–Cahn–Hilliard-like equations with bending forces. We derive this model using the Lagrange–d’Alembert principle considering various dissipation mechanisms. The highly nonlinear model is solved numerically to explore the tight interplay between surface evolution, surface phase composition, surface curvature and surface hydrodynamics. It is demonstrated that hydrodynamics can enhance bulging and furrow formation, which both can further develop to pinch-offs. The numerical approach builds on a Taylor–Hood element for the surface Navier–Stokes part, a semi-implicit approach for the Cahn–Hilliard part, higher-order surface parametrizations, appropriate approximations of the geometric quantities, and mesh redistribution. We demonstrate convergence properties that are known to be optimal for simplified subproblems.

Key words: biological fluid dynamics, interfacial flows (free surface), mathematical foundations

1. Introduction

Coexisting fluid domains in biomembranes and in their model systems is an intensively studied field of research. With the possibility to visualize coexisting lipid phases in model membranes by high-resolution fluorescence imaging (Baumgart, Hess & Webb 2003) a strong correlation between domain composition and local membrane curvature can be established. These findings have supported earlier membrane models (Jülicher &

† Email address for correspondence: axel.voigt@tu-dresden.de

‡ Present address: Department of Mathematics ‘Tullio Levi-Civita’, University of Padua, Italy.

Lipowsky 1996; Jiang, Lookman & Saxena 2000; Kumar, Gompper & Lipowsky 2001) and initiated a wealth of theoretical, numerical and experimental studies to understand the relation between composition and curvature (Baumgart *et al.* 2003, 2005; Veatch & Keller 2003; Veatch *et al.* 2007; Wang & Du 2008; Lowengrub, Rätz & Voigt 2009; Elliott & Stinner 2010*b*; Elson *et al.* 2010; Garcke *et al.* 2016; Gera & Salac 2018; Zimmermann *et al.* 2019). This relation has strong biological implications (McMahon & Gallop 2005). We refer to Veatch & Keller (2003), Deserno (2015) and Lipowsky & Dimova (2021) for reviews on the subject. While most studies address multicomponent giant unilaminar vesicles and consider phase separation and coarsening on spherical shapes, more recently multicomponent scaffolded lipid vesicles have been considered. In these systems, non-spherical shapes are stabilized and the effect of spatially varying curvature on phase separation and coarsening has been considered (Fonda *et al.* 2018, 2019; Rinaldin *et al.* 2020). These results demonstrate the strong influence of curvature on the spatial arrangement of the lipid phases. On the other hand also the shape evolution is considered. Coexisting fluid domains can lead to bulging and budding events (Baumgart *et al.* 2003; Lowengrub *et al.* 2009; Elliott & Stinner 2010*b*), indicating also the strong influence of composition on the evolving shape. Thus, the correlation between domain composition and membrane curvature acts in both directions. These effects can essentially be modelled by the Jülicher–Lipowsky model (Jülicher & Lipowsky 1996) or appropriate phase field approximations of it (Lowengrub *et al.* 2009; Haußer *et al.* 2013). These models essentially extend the classical Helfrich model to multiple components. Instead of a simple L^2 -gradient flow of the Helfrich energy, with possible constraints, the model allows for dissipation through the simultaneous evolution of the shape and the lipid phases on the surface. Such models can be embedded in bulk flows and serve as interfacial conditions (Sohn *et al.* 2010; Zhang & Wolgemuth 2022). However, all these studies neglect the effect of surface viscosity. Surface viscosity has been shown to be a key property of biomembranes and their model systems controlling remodelling and with it, the coarsening process, see (Faizi, Dimova & Vlahovska 2022) for discussions and measurements. Already for flat membranes, it has been shown that experimental results on the coarsening rate of these fluid domains can only be quantitatively reproduced by simulations if the fluid properties of the membrane are taken into account (Fan, Han & Haataja 2010; Camlay & Brown 2011). Considering these effects on curved surfaces involves several modelling and numerical subtleties, due to the increased coupling between local curvature and surface fluid velocity. Although there are models in the literature dealing with the coupling between surface flow on curved surfaces and the surrounding bulk flow (Woodhouse & Goldstein 2012; Barrett, Garcke & Nürnberg 2015; Reuther & Voigt 2016), they do not consider coexisting fluid domains. Furthermore, it has been shown that the effect of the bulk fluid can be neglected if the Saffman–Delbrück number (Saffman & Delbrück 1975), which defines a hydrodynamic length relating the viscosity of the membrane and the surrounding bulk fluid, is large. In this case the hydrodynamics is effectively two-dimensional (2-D) on spatial scales smaller than the Saffman–Delbrück number (Henle & Levine 2010). We follow this simplification and consider only surface two-phase flow problems. On stationary surfaces these problems are addressed in Nitschke, Voigt & Wensch (2012), Ambrus *et al.* (2019), Olshanskii, Palzhanov & Quaini (2022) and Bachini, Krause & Voigt (2023*b*) and essentially reveal an enhanced coarsening rate due to hydrodynamic effects, similar to the situation in flat space (Fan *et al.* 2010; Camlay & Brown 2011). To consider evolving surfaces under the influence of surface viscosity requires models for so-called fluid deformable surfaces. Such models have been established as model systems for biomembranes (Arroyo & DeSimone 2009;

Torres-Sánchez, Millán & Arroyo 2019). They exhibit a solid–fluid duality, while they store elastic energy when stretched or bent, as solid shells, they flow as viscous 2-D fluids under in-plane shear. This duality has several consequences: it establishes a tight interplay between tangential flow and surface deformation. In the presence of curvature, any shape change is accompanied by a tangential flow and, *vice versa*, the surface deforms due to tangential flow. Models describing this interplay between curvature and surface flow have been introduced and numerically solved in Torres-Sánchez *et al.* (2019), Reuther, Nitschke & Voigt (2020) and Krause & Voigt (2023). These numerical approaches provide the basis to explore the impact of surface viscosity on the dynamics of biomembranes. We here extend these models to two-phase flows by combining fluid deformable surfaces with a phase field approximation of the Jülicher–Lipowsky model. The model is systematically derived by a Lagrange–d’Alembert principle, accounting for dissipation by domain coarsening, shape evolution and surface viscosity. We relate the resulting model to known simplified models in the literature. We provide a detailed description of the numerical approach, which uses surface finite elements (SFEM) (Dziuk & Elliott 2013; Nestler, Nitschke & Voigt 2019) and builds on previous developments for one-component fluid deformable surfaces (Krause & Voigt 2023) and surface Navier–Stokes–Cahn–Hilliard-like models on stationary surfaces (Bachini *et al.* 2023*b*). The algorithm is used to demonstrate the strong interplay between composition, curvature and hydrodynamics and its implications for bulging and budding processes. Measuring the essential material properties, surface viscosity and bending rigidity for biomembranes is a challenging task, see (Faizi *et al.* 2022). Reported parameters vary by orders of magnitude. We therefore are not considering a specific system but the general properties by exploring the parameter space. Briefly, surface hydrodynamics enhances the onset of shape deformations and possible resulting topological changes, which has strong biological implications, e.g. in the case of endocytosis and exocytosis (Kaksonen & Roux 2018; Al-Izzi, Sens & Turner 2020).

The paper is structured as follows. In § 2 we introduce the used notation necessary to formulate the surface model, briefly describe the model derivation, formulate the two-phase fluid deformable surface model and relate the equations to known simplified models. Details are considered in the appendices. In § 3 we discuss the considered numerical approach. In § 4 we provide all used parameters, consider convergence studies and explore the parameter space and the implications of the coupling between composition, shape and surface flow. In § 5 we draw conclusions.

2. Continuous model

We derive the full model for two-phase fluid deformable surfaces by applying the Lagrange–d’Alembert principle. We first introduce the necessary notation, then motivate the use of the Lagrange–d’Alembert principle, introduce all ingredients and derive the model. Finally, we relate the model to known simplifications in the literature.

2.1. Notation

We consider a time dependent smooth and oriented surface $\mathcal{S} = \mathcal{S}(t)$ without boundary. Related to \mathcal{S} , we denote the outward pointing surface normal \mathbf{v} , the surface projection $\mathbf{P} = \mathbf{I} - \mathbf{v} \otimes \mathbf{v}$, the shape operator $\mathcal{B} = -\nabla_{\mathbf{P}}\mathbf{v}$ and the mean curvature $\mathcal{H} = \text{tr}\mathcal{B}$. Note that, under these definitions the unit sphere has negative mean curvature $\mathcal{H} = -2$. Let ϕ be a continuously differentiable scalar field, \mathbf{u} a continuously differentiable \mathbb{R}^3 -vector field, and σ a continuously differentiable $\mathbb{R}^{3 \times 3}$ -tensor field defined on \mathcal{S} . We define

the surface tangential gradient ∇_P as in Jankuhn, Olshanskii & Reusken (2018) and the componentwise surface gradient ∇_C as in Nitschke, Sadik & Voigt (2022), namely

$$\left. \begin{aligned} \nabla_P \phi &= P \nabla \phi^e, \\ \nabla_P \mathbf{u} &= P \nabla \mathbf{u}^e P, \\ \nabla_C \boldsymbol{\sigma} &= \nabla \boldsymbol{\sigma}^e P, \end{aligned} \right\} \quad (2.1)$$

where ϕ^e , \mathbf{u}^e and $\boldsymbol{\sigma}^e$ are arbitrary smooth extensions of ϕ , \mathbf{u} and $\boldsymbol{\sigma}$ in the normal direction and ∇ is the gradient of the embedding space \mathbb{R}^3 . The fields $\nabla_P \phi$, $\nabla_P \mathbf{u}$ are purely tangential vector and tensor fields, respectively. We define the corresponding divergence operators for a vector field \mathbf{u} and a tensor field $\boldsymbol{\sigma}$ by

$$\left. \begin{aligned} \operatorname{div}_P \mathbf{u} &= \operatorname{tr}(\nabla_P \mathbf{u}), \\ \operatorname{div}_C(\boldsymbol{\sigma} P) &= \operatorname{tr} \nabla_C(\boldsymbol{\sigma} P), \end{aligned} \right\} \quad (2.2)$$

where tr is the trace operator. The divergence of the tensor $\boldsymbol{\sigma}$, $\operatorname{div}_C \boldsymbol{\sigma}$, leads to a non-tangential vector field even if $\boldsymbol{\sigma}$ is a tangential tensor field. Let ∇_S be the gradient with respect to the covariant derivative on \mathcal{S} , as used in Reuther *et al.* (2020). This operator is defined for scalar fields and tangential vector fields and relates to the tangential operators by $\nabla_P \phi = \nabla_S \phi$ and $\operatorname{div}_P \mathbf{u} = \operatorname{div}_S(P\mathbf{u}) - (\mathbf{u} \cdot \boldsymbol{\nu})\mathcal{H}$, respectively. We further clarify the relation between the above operators in Appendix A.

The surface \mathcal{S} is given by a parametrization X . The material on the surface is described by a material parametrization X_m , as in Nitschke & Voigt (2022). Both parametrizations relate to each other by $\partial_t X_m \cdot \boldsymbol{\nu} = \partial_t X \cdot \boldsymbol{\nu}$, which leads to a Lagrangian perspective in normal direction. In tangential direction the surface and the material can move independently. We define the material velocity by $\mathbf{u} := \partial_t X_m$ and the relative material velocity by $\mathbf{w} := \mathbf{u} - \partial_t X$. The relative material velocity is a pure tangential vector field. Additional information and the relation to the time derivative used can be found in Appendix B.6.

2.2. Model derivation by the Lagrange–d’Alembert principle

The Lagrange–d’Alembert principle has been explained in Marsden & Ratiu (2013). The approach is a combination of the Lagrange and the Onsager variational principles. The concept of the Lagrange principle has been introduced in Marsden & West (2001), Marsden & Ratiu (2013) and Hairer *et al.* (2006) and it models the interplay of kinetic and potential energies under total energy conservation. On the other side, the concept of the Onsager variational principle models dissipative systems, where potential energy decreases under a dissipation potential, e.g. L^2 -gradient flows. Within our context, the Onsager principle is used in Torres-Sánchez *et al.* (2019) to derive fluid deformable surfaces with the surface Stokes model.

We consider a density function ϕ that describes the two-phases on the surface \mathcal{S} , e.g. liquid-ordered and disordered phases, where one phase is represented by $\phi = 1$, the other one by $\phi = -1$, and we assume a mixture of both if $\phi \in (-1, 1)$. We consider a conserved evolution for ϕ with respect to the following energies.

The first is a Ginzburg–Landau energy modelling phase-separation on \mathcal{S} ,

$$\mathcal{F}_{GL} = \int_{\mathcal{S}} \tilde{\sigma} \left(\frac{\epsilon}{2} \|\nabla_S \phi\|^2 + \frac{1}{\epsilon} W(\phi) \right) d\mathcal{S}, \quad (2.3)$$

where $\tilde{\sigma} > 0$ is a rescaled line tension with $\tilde{\sigma} = 3/(2\sqrt{2})\sigma$, σ the line tension in the corresponding Jülicher–Lipowski model (Garcke *et al.* 2016; Elliott, Hatcher &

Stinner 2022; Benes *et al.* 2023), $\epsilon > 0$ is related to the diffuse interface width and $W(\phi) = \frac{1}{4}(\phi^2 - 1)^2$ is a double-well potential.

The second energy we consider accounts for bending properties. As in Fonda *et al.* (2018) and Bachini *et al.* (2023b), we consider a diffuse interface approximation of the Jülicher–Lipowski model (Jülicher & Lipowsky 1996),

$$\mathcal{F}_H = \int_S \frac{1}{2} \kappa(\phi) (\mathcal{H} - \mathcal{H}_0(\phi))^2 dS, \tag{2.4}$$

where $\kappa(\phi)$ is the bending stiffness and $\mathcal{H}_0(\phi)$ the spontaneous curvature. We neglect additional contributions due to the Gaussian curvature of \mathcal{S} . This is justified as long as the Gaussian bending stiffness is independent on the phase ϕ and no topological changes occur. To get a continuously differentiable dependency on ϕ we consider an interpolation function as in Elliott & Stinner (2010b) and Bachini *et al.* (2023b),

$$f(\phi) = \begin{cases} f_1 & \text{if } \phi = 1, \\ \frac{f_1 + f_2}{2} + \frac{f_1 - f_2}{4} \phi(3 - \phi^2) & \text{if } -1 < \phi < 1, \\ f_2 & \text{if } \phi = -1, \end{cases} \tag{2.5}$$

for $f \in \{\kappa, \mathcal{H}_0\}$ and f_1, f_2 the material parameter of κ or \mathcal{H}_0 in the separated phases. Together, the energies \mathcal{F}_{GL} and \mathcal{F}_H define the potential energy $\mathcal{F} = \mathcal{F}_H + \mathcal{F}_{GL}$ of the system.

We define the surface material velocity by \mathbf{u} and the kinetic energy as in Reuther *et al.* (2020) by

$$\mathcal{F}_K = \int_S \frac{\rho}{2} \|\mathbf{u}\|^2 dS, \tag{2.6}$$

with ρ the surface density. For simplicity, we assume ρ to be constant. The Lagrangian $\mathcal{L} = \mathcal{F}_K - \mathcal{F}$ is defined as the difference between the kinetic and the potential energy.

We next consider the various sources of dissipation. As in Torres-Sánchez *et al.* (2019) we define the dissipation potential of the viscous stress,

$$\mathcal{D}_V = \int_S \eta \|\boldsymbol{\sigma}\|^2, \tag{2.7}$$

where η denotes the viscosity and $\boldsymbol{\sigma}(\mathbf{u}) = \frac{1}{2}(\nabla \mathbf{p} \mathbf{u} + (\nabla \mathbf{p} \mathbf{u})^T)$ is the rate of deformation tensor as considered in Jankuhn *et al.* (2018). For simplicity, we assume η to be constant. In addition, we consider the friction with the surrounded material, which is modelled by

$$\mathcal{D}_R = \int_S \frac{\gamma}{2} \|\mathbf{u}\|^2, \tag{2.8}$$

where $\gamma \geq 0$ is a friction coefficient, again assumed to be constant. The third component of the dissipation potential is associated with the dissipation due to phase separation. We assume the immobility potential of the phase field given by

$$\mathcal{D}_\phi = \int_S \frac{1}{2m} \|\dot{\phi}\|_{H^{-1}}^2, \tag{2.9}$$

with $m > 0$ a resistance associated with $\dot{\phi} = \partial_t \phi + \nabla_w \phi$ with respect to H^{-1} norm. Thereby, $\dot{\phi}$ denotes the material time derivative of ϕ and $\nabla_w \phi = (\nabla_S \phi, \mathbf{w})$, see

Appendix B.6. The parameter m plays the role of a mobility. Here, we follow the approach of Magaletti *et al.* (2013) and consider this parameter to be constant. For alternative approaches, we refer to Abels (2009). We now define the dissipation potential by $\mathcal{D} = \mathcal{D}_V + \mathcal{D}_R + \mathcal{D}_\phi$.

Moreover, we add to \mathcal{L} and \mathcal{D} the following constraints. We here only assume local inextensibility of the material as in Torres-Sánchez *et al.* (2019) and Reuther *et al.* (2020). This is incorporated by the Lagrange-function p , which serves as the surface pressure and is related to the surface tension. It enters in the constraint by

$$\mathcal{C}_{IE} = - \int_S p \operatorname{div} \mathbf{p} \mathbf{u}. \tag{2.10}$$

This constraint induces a conservation of surface area $|\mathcal{S}|$. We neglect possible additional constraints, e.g. on the enclosed volume.

With these ingredients, the Lagrange–d’Alembert principle can be applied. The concept is introduced and used for rigid body models in Marsden & West (2001), Udewadia & Kalaba (2002) and Izadi & Sanyal (2014). Here we consider this principle for space-dependent functions, for which it provides an elegant way to derive thermodynamically consistent models. It reads

$$0 = (\rho(\partial_t \mathbf{u} + \nabla_{\mathbf{w}} \mathbf{u}) + \mathbf{D}_X \mathcal{F} + \mathbf{D}_u \mathcal{D} + \mathbf{D}_u \mathcal{C}_{IE}, \mathbf{Y}) + (\mathbf{D}_\phi \mathcal{F} + \mathbf{D}_\phi \mathcal{D}, \psi) + (\mathbf{D}_p \mathcal{C}_{IE}, q), \tag{2.11}$$

for all test functions $\mathbf{Y} \in T\mathbb{R}^3|_S$ and $\psi, q \in T^0\mathcal{S}$. Here, the symbol \mathbf{D} denotes the L^2 -gradient of the functional. See Appendix B for the explicit definitions and calculations. The approach is broadly applicable and provides an alternative to other frameworks, such as the Onsager principle. We obtain the following problem.

PROBLEM 2.1. Find $(\mathbf{u}, p, \phi, \mu)$ such that

$$\left. \begin{aligned} \partial_t \phi + \nabla_{\mathbf{w}} \phi &= m \Delta_S \mu, \\ \mu &= \tilde{\sigma} \left(-\epsilon \Delta_S \phi + \frac{1}{\epsilon} W'(\phi) \right) + \frac{1}{2} \kappa'(\phi) (\mathcal{H} - \mathcal{H}_0(\phi))^2 \\ &\quad - \kappa(\phi) \mathcal{H}'_0(\phi) (\mathcal{H} - \mathcal{H}_0(\phi)), \\ \rho(\partial_t \mathbf{u} + \nabla_{\mathbf{w}} \mathbf{u}) &= -\nabla_S p - p \mathcal{H} \mathbf{v} + 2\eta \operatorname{div}_C \boldsymbol{\sigma} - \gamma \mathbf{u} + \mathbf{b}_T + \mathbf{b}_N, \\ \operatorname{div} \mathbf{p} \mathbf{u} &= 0, \end{aligned} \right\} \tag{2.12}$$

with tangential and normal bending forces defined by

$$\left. \begin{aligned} \mathbf{b}_T &= \mu \nabla_S \phi, \\ \mathbf{b}_N &= - \left(\Delta_S (\kappa(\phi) (\mathcal{H} - \mathcal{H}_0(\phi))) + \kappa(\phi) (\mathcal{H} - \mathcal{H}_0(\phi)) \right. \\ &\quad \left. \times \left(\|\mathcal{B}\|^2 - \frac{1}{2} \mathcal{H} (\mathcal{H} - \mathcal{H}_0(\phi)) \right) \right) \mathbf{v} \\ &\quad + \tilde{\sigma} \left(\frac{\epsilon}{2} \|\nabla_S \phi\|^2 + \frac{1}{\epsilon} W(\phi) \right) \mathcal{H} \mathbf{v} - \tilde{\sigma} \epsilon \nabla_S \phi^T \mathcal{B} \nabla_S \phi \mathbf{v}, \end{aligned} \right\} \tag{2.13}$$

and \mathbf{w} the relative material velocity as explained above.

This problem provides a tight coupling between the phase field ϕ , the surface velocity \mathbf{u} , the surface pressure p and the geometry \mathcal{S} . Exploring the main implications of these couplings is one of the goals of this paper.

REMARK 2.1 (Thermodynamic consistency). We refer to [Appendix B.5](#) to show that the relation

$$\frac{d}{dt}(\mathcal{F}_K + \mathcal{F}) = -2\mathcal{D} \leq 0, \quad (2.14)$$

holds for the model in [Problem 2.1](#). This demonstrates thermodynamic consistency.

Considering a characteristic length and a characteristic velocity, [Problem 2.1](#) can be formulated in non-dimensional form, see [Appendix C](#) for details. Keeping the same notation also in non-dimensional form, we obtain the following.

PROBLEM 2.2. Find $(\mathbf{u}, p, \phi, \mu)$ such that

$$\partial_t \phi + \nabla_w \phi = m \Delta_S \mu, \quad (2.15)$$

$$\begin{aligned} \mu = \tilde{\sigma} \left(-\epsilon \Delta_S \phi + \frac{1}{\epsilon} W'(\phi) \right) + \frac{1}{2} \kappa'(\phi) (\mathcal{H} - \mathcal{H}_0(\phi))^2 \\ - \kappa(\phi) \mathcal{H}'_0(\phi) (\mathcal{H} - \mathcal{H}_0(\phi)), \end{aligned} \quad (2.16)$$

$$\partial_t \mathbf{u} + \nabla_w \mathbf{u} = -\nabla_S p - p \mathcal{H} \mathbf{v} + \frac{2}{Re} \operatorname{div}_C \boldsymbol{\sigma} - \gamma \mathbf{u} + \mathbf{b}_T + \mathbf{b}_N, \quad (2.17)$$

$$\operatorname{div}_p \mathbf{u} = 0, \quad (2.18)$$

where Re denotes the Reynolds number and \mathbf{b}_T and \mathbf{b}_N are defined as in [Problem 2.1](#).

In this form, the problem is suitable for numerical approximation. However, before addressing the model in its discrete form, we consider several model simplifications.

2.3. Model simplifications

The model in [Problem 2.2](#) is a two-component fluid deformable surface model with phase-dependent elasticity. For simplicity, we assume that the material parameters, such as the density ρ , the viscosity η and the friction coefficient γ , are constant. It is possible to extend the model and consider phase-dependent parameters by following the approach described, for example, in [Lowengrub & Truskinovsky \(1998\)](#), [Abels, Garcke & Grün \(2012\)](#), [Aland & Voigt \(2012\)](#) and [Ten Eikelder *et al.* \(2023\)](#). In the following, we link our model to simplified models already discussed in the literature.

2.3.1. One component fluid deformable surface

In the case of a single phase, the simplified model considers only surface hydrodynamics and its interaction with the geometry due to bending. Explicitly, by considering $\phi \equiv \text{const}$,

the system simplifies to

$$\left. \begin{aligned} \partial_t \mathbf{u} + \nabla_{\mathbf{w}} \mathbf{u} &= -\nabla_S p - p \mathcal{H} \mathbf{v} + \frac{2}{Re} \operatorname{div}_C \boldsymbol{\sigma} - \gamma \mathbf{u} + \mathbf{b}_N, \\ \operatorname{div}_P \mathbf{u} &= 0, \end{aligned} \right\} \quad (2.19)$$

where $\mathbf{w} = \mathbf{u} - \partial_t \mathbf{X}$ as before, and the normal bending forces reduce to

$$\mathbf{b}_N = -\kappa (\Delta_S \mathcal{H} + (\mathcal{H} - \mathcal{H}_0) (\|\mathcal{B}\|^2 - \frac{1}{2} \mathcal{H} (\mathcal{H} - \mathcal{H}_0))) \mathbf{v}. \quad (2.20)$$

Note that, bending stiffness and spontaneous curvature are now constant parameters. In the case of $\mathcal{H}_0 = 0$ and $\gamma = 0$, this model has been introduced and simulated in Reuther *et al.* (2020), Krause & Voigt (2023) and in the Stokes limit in Torres-Sánchez *et al.* (2019). For further numerical and analytical approaches under additional symmetry assumptions we refer to Al-Izzi *et al.* (2020), where a linear stability analysis of a tube geometry is considered, and to Olshanskii (2023), where potential rotational symmetric equilibrium configurations are addressed. For a comparison of different derivations of this model we refer to Reuther & Voigt (2015, 2018a) and Brandner, Reusken & Schwering (2022b).

2.3.2. Two-component fluid on a stationary surface

If we assume a stationary surface \mathcal{S} , i.e. $\mathbf{u} \cdot \mathbf{v} = 0$, the model in Problem 2.2 restricts to a pure tangential problem. We follow the approach of the directional splitting as shown in detail in Jankuhn *et al.* (2018) and used in Reuther *et al.* (2020). We note that $\mathbf{u}_T = P\mathbf{u}$ and $u_N = \mathbf{u} \cdot \mathbf{v}$ for the tangential and normal surface velocity, respectively. We project the equations in the surface tangent space and this results in a surface two-phase flow problem,

$$\left. \begin{aligned} \partial_t \phi + \nabla_{\mathbf{w}} \phi &= m \Delta_S \mu, \\ \mu &= \tilde{\sigma} \left(-\epsilon \Delta_S \phi + \frac{1}{\epsilon} W'(\phi) \right) + \frac{1}{2} \kappa'(\phi) (\mathcal{H} - \mathcal{H}_0(\phi))^2 \\ &\quad - \kappa(\phi) \mathcal{H}'_0(\phi) (\mathcal{H} - \mathcal{H}_0(\phi)), \\ P \partial_t \mathbf{u}_T + \nabla_{\mathbf{w}} \mathbf{u}_T &= -\nabla_S p + \frac{2}{Re} \operatorname{div}_S \boldsymbol{\sigma}(\mathbf{u}_T) - \gamma \mathbf{u}_T + \mu \nabla_S \phi, \\ \operatorname{div}_S \mathbf{u}_T &= 0, \end{aligned} \right\} \quad (2.21)$$

where the relative material velocity simplifies to the Eulerian case $\mathbf{w} = \mathbf{u}_T$. Because of the tangentiality of the vector and tensor fields, all differential operators fall back to the operators with respect to the covariant derivative. In the case of $\gamma = 0$, the model has been introduced and discussed in Bachini *et al.* (2023b), where it is used to study the influence of surface hydrodynamics on coarsening in multicomponent scaffolded lipid vesicles, see Fonda *et al.* (2018), Fonda *et al.* (2019) and Rinaldin *et al.* (2020). Without the bending terms, the system has already been addressed in Nitschke *et al.* (2012), Ambrus *et al.* (2019) and Olshanskii *et al.* (2022).

2.3.3. One component fluid on a stationary surface

By considering a single phase on a stationary surface, the system simplifies even further and leads to the inextensible surface Navier–Stokes equations on a stationary surface,

$$\left. \begin{aligned} P\partial_t \mathbf{u}_T + \nabla_{\mathbf{w}} \mathbf{u}_T &= -\nabla_{SP} + \frac{2}{Re} \operatorname{div}_S \boldsymbol{\sigma}(\mathbf{u}_T) - \gamma \mathbf{u}, \\ \operatorname{div}_S \mathbf{u} &= 0, \end{aligned} \right\} \quad (2.22)$$

where again $\mathbf{w} = \mathbf{u}_T$. These equations have been solved numerically for simply connected surfaces in Nitschke *et al.* (2012) and Reuther & Voigt (2015, 2018a) (and in the Stokes limit in Olshanskii *et al.* (2018), Bonito, Demlow & Licht (2020) and Brandner & Reusken (2020)), and for general surfaces in Nitschke, Reuther & Voigt (2017), Reusken (2018), Fries (2018), Reuther *et al.* (2020), Reuther & Voigt (2018b) and Lederer, Lehrenfeld & Schoeberl (2020) (and in the Stokes limit in Olshanskii & Yushutin (2019)).

2.3.4. Two-component surface without fluid behaviour

A larger literature exists for the evolution of two-component surfaces if surface hydrodynamics is neglected. These models are related to the overdamped limit of Problem 2.2. An explicit derivation is shown in Appendix D. The resulting model reads

$$\left. \begin{aligned} \partial_t \phi + \nabla_{\mathbf{w}} \phi &= \tilde{m} \Delta_S \tilde{\mu}, \\ \tilde{\mu} &= -\tilde{\sigma} \epsilon \Delta_S \phi + \frac{\tilde{\sigma}}{\epsilon} W'(\phi), \\ &\quad + \frac{1}{2} \tilde{\kappa}'(\phi) (\mathcal{H} - \mathcal{H}_0(\phi))^2 - \tilde{\kappa}(\phi) \mathcal{H}'_0(\phi) (\mathcal{H} - \mathcal{H}_0(\phi)), \\ u_N &= -\tilde{p} \mathcal{H} + \tilde{b}_N, \\ \mathbf{u}_T &= -\nabla_S \tilde{p} + \tilde{\mu} \nabla_S \phi, \\ -\Delta_S \tilde{p} + \tilde{p} \mathcal{H}^2 &= -\operatorname{div}_S(\tilde{\mu} \nabla_S \phi) + b_N \mathcal{H}, \end{aligned} \right\} \quad (2.23)$$

where $\tilde{b}_N = \tilde{\mathbf{b}}_N \cdot \mathbf{v}$. In this model, \tilde{p} serves as a Lagrange function to ensure the local inextensibility constraint. The model is similar to a model discussed in Haußer *et al.* (2013), see Appendix D for a detailed comparison. If the constraint on local inextensibility is dropped and only a global area constraint is considered, the model further simplifies. See Appendix D for the relations with the models considered in Wang & Du (2008) and Elliott & Stinner (2010a), which are derived by only considering variations in the normal direction. One essential difference is the tangential velocity component $\tilde{\mu} \nabla_S \phi$, which is not present in these models. We consider the model in Elliott & Stinner (2010a) but with an additional local inextensibility constraint for a qualitative comparison to highlight the differences of the model derivation and the importance of surface hydrodynamics on the evolution of two-component membranes.

3. Numerical discretization

We consider a SFEM (Dziuk & Elliott 2013; Nestler *et al.* 2019) to solve the highly nonlinear set of geometric and surface partial differential equations (PDEs) in Problem 2.2. The approach uses higher-order surface discretizations, mesh regularization, a Taylor–Hood element for the surface Navier–Stokes equations and established approaches

in flat space to split the Navier–Stokes–Cahn–Hilliard-like problem. The discretization on the surface addresses numerical analysis results for vector-valued surface PDEs ensuring convergence of surface vector-Laplace and surface Stokes problems on stationary surfaces (Hansbo, Larson & Larsson 2020; Hardering & Praetorius 2022) and reproduces the same expected optimal order of convergences for the full two-component fluid deformable surface model.

3.1. Mesh movement

By following the work in Krause & Voigt (2023), we combine the system in Problem 2.2 with a mesh redistribution approach introduced in detail in Barrett, Garcke & Nürnberg (2008). We consider the initial surface given $X(0) = X_0$ and an additional equation for the time evolution of the parametrization

$$\partial_t X \cdot \mathbf{v} = \mathbf{u} \cdot \mathbf{v}, \tag{3.1}$$

$$\mathcal{H}\mathbf{v} = \Delta_C X. \tag{3.2}$$

This approach generates a tangential mesh movement that maintains the shape regularity and additionally provides an implicit representation of the mean curvature \mathcal{H} .

3.2. Surface approximation

We assume that the smooth surface \mathcal{S} is approximated by a discrete k th-order approximation \mathcal{S}_h . Let \mathcal{S}_h^{lin} be a piecewise linear reference surface given by shape regular triangulation $\mathcal{T}_h^{lin} = \{T_i\}_{i=1}^{N_T}$. We define X as bijective map $X: \mathcal{S}_h^{lin} \rightarrow \mathcal{S}$ such that $\mathcal{S} = \cup_{i=1}^{N_T} X(T_i)$. The construction of such maps is discussed in Praetorius & Stenger (2020) and Brandner *et al.* (2022a). We get a k th-order approximation of X by the k th-order interpolation $\mathcal{S}_h^k = I_h^k(X)$, which defines a higher-order triangulation such that $\mathcal{S}_h^k = \cup_{i=1}^{N_T} X_h^k(T_i)$. We use each geometrical quantity like the normal vector \mathbf{v}_h , the shape operator \mathcal{B}_h and the inner products $(\cdot, \cdot)_h$ with respect the \mathcal{S}_h^k where we will drop the index k in the following. We denote the size of the grid by h , i.e. the longest edge of the mesh.

3.3. Discrete function spaces and weak formulation

We define the discrete function spaces for scalar function by

$$V_{k_e}(\mathcal{S}_h) = \{\psi \in C^0(\mathcal{S}_h) | \psi|_T \in \mathcal{P}_{k_e}(T)\}, \tag{3.3}$$

with \mathcal{P}_{k_e} the space polynomials, where we set the element order as $k_e = k$. We define $V_k(\mathcal{S}_h) = [V_k(\mathcal{S}_h)]^3$ as space of discrete vector fields. We discretize $\mathbf{u}_h, X_h \in V_2(\mathcal{S}_h)$, $\mathcal{H}_h, \phi_h, \mu_h \in V_2(\mathcal{S}_h)$ and $p_h \in V_1(\mathcal{S}_h)$. This corresponds to a Taylor–Hood element for the pair of velocity and pressure. The resulting weak formulation reads

$$(\partial_t \phi_h + \nabla_{w_h} \phi_h, \psi_h)_h = -m(\nabla_S \mu, \nabla_S \psi_h)_h, \tag{3.4}$$

A two-phase fluid deformable surface model

$$\begin{aligned}
 (\mu_h, \xi_h) &= \tilde{\sigma} \epsilon (\nabla_S \phi_h, \nabla_S \xi_h)_h - \frac{\tilde{\sigma}}{\epsilon} (W'(\phi_h), \xi_h)_h \\
 &\quad + \frac{1}{2} (\kappa'(\phi_h) (\mathcal{H}_h - \mathcal{H}_0(\phi_h))^2, \xi_h)_h \\
 &\quad - (\kappa(\phi_h) \mathcal{H}'_0(\phi_h) (\mathcal{H}_h - \mathcal{H}_0(\phi_h)), \xi_h)_h, \tag{3.5}
 \end{aligned}$$

$$(\partial_t \mathbf{u}_h + \nabla_{\mathbf{w}_h} \mathbf{u}_h, \mathbf{v}_h)_h = (p_h, \operatorname{div}_P \mathbf{v}_h)_h - \frac{2}{Re} (\boldsymbol{\sigma}_h, \nabla_P \mathbf{v}_h)_h + (\mathbf{b}_T + \mathbf{b}_N - \gamma \mathbf{u}_h, \mathbf{v}_h)_h, \tag{3.6}$$

$$(\operatorname{div}_P \mathbf{u}_h, q_h)_h = 0, \tag{3.7}$$

$$(\partial_t \mathbf{X}_h \cdot \mathbf{v}_h, h_h)_h = (\mathbf{u}_h \cdot \mathbf{v}_h, h_h)_h, \tag{3.8}$$

$$(\mathcal{H}_h \mathbf{v}_h, \mathbf{Z}_h)_h = -(\nabla_C \mathbf{X}_h, \nabla_C \mathbf{Z}_h)_h, \tag{3.9}$$

for all $(\psi_h, \xi_h, \mathbf{v}_h, q_h, h_h, \mathbf{Z}_h) \in [V_k \times V_k \times V_k \times V_{k-1} \times V_k \times V_k](\mathcal{S}_h)$.

3.4. Discrete model

Following the strategy in Bachini *et al.* (2023b), we separate the surface phase field equations (3.4)–(3.5) and surface Navier–Stokes equations (3.6)–(3.7) by an operator-splitting approach. In 2-D and three-dimensional (3-D) settings such splitting approaches are common strategies for Navier–Stokes–Cahn–Hilliard systems, and have been shown to be robust and fast converging, see, for example, Demont *et al.* (2022) for a detailed analysis. Similar properties have been found in Bachini *et al.* (2023b) on surfaces. In contrast to Bachini *et al.* (2023b), where the surface was stationary, here the surface evolves and we adapt the numerical schemes used in Krause & Voigt (2023) for one-component systems.

Let $\{t^n\}_i^N$ be time interval discretization, with $t^n = n\tau$ and $\tau > 0$ be the time steps. We first solve the surface phase field problem (3.4)–(3.5), and then solve the surface Navier–Stokes (3.6) and (3.7), together with (3.8)–(3.9) for mesh regularization. The inner product $(\cdot, \cdot)_h$ is approximated by a quadrature rule with an order that is chosen high enough such that test and trial functions and area elements are well integrated. We denote the time discrete surface by $\mathcal{S}_h^{n-1} = \mathcal{S}_h(t^{n-1})$.

The equations are discretized in time by a semi-implicit Euler scheme where the nonlinear terms are chosen explicitly apart from the double well potential. As is common for Cahn–Hilliard equations, we linearize the derivative of the double-well potential by a Taylor expansion of order one.

PROBLEM 3.1 (Discrete surface Cahn–Hilliard problem). *Find $(\phi_h, \mu_h) \in [V_h \times V_h](\mathcal{S}_h^{n-1})$ such that*

$$\left. \begin{aligned}
 &\frac{1}{\tau} (\phi_h^n, \psi_h)_h + (\nabla_{\mathbf{w}^{n-1}} \phi_h^n, \psi_h)_h = \frac{1}{\tau} (\phi_h^{n-1}, \psi_h)_h - m (\nabla_S \mu_h^n, \nabla_S \psi_h)_h, \\
 &(\mu_h^n, \xi_h)_h = \epsilon (\nabla_S \phi_h^n, \nabla_S \xi_h)_h + \frac{1}{\epsilon} (-2(\phi_h^{n-1})^3 + (3(\phi_h^{n-1})^2 - 1)\phi_h^n, \xi_h)_h \\
 &\quad + \frac{1}{2} (\kappa'(\phi_h^{n-1}) (\mathcal{H}_h^{n-1} - \mathcal{H}_0(\phi_h^{n-1}))^2, \xi_h)_h \\
 &\quad - (\kappa(\phi_h^{n-1}) \mathcal{H}'_0(\phi_h^{n-1}) (\mathcal{H}_h^{n-1} - \mathcal{H}_0(\phi_h^{n-1})), \xi_h)_h
 \end{aligned} \right\} \tag{3.10}$$

for all $(\psi_h, \xi_h) \in [V_h \times V_h](\mathcal{S}_h^{n-1})$.

This approach can be related to analysed schemes for the Cahn–Hilliard and Navier–Stokes–Cahn–Hilliard equations with explicit treatment of the double-well potential and additional stabilization terms, for example, Shen & Yang (2010a,b). These methods and more an advanced scalar auxiliary variable (SAV) approaches, for example, Zhu *et al.* (2019), have been shown to be unconditionally energy-stable in 2-D and 3-D settings.

The surface Navier–Stokes equations and the mesh redistribution are considered together. Moreover, we define a discrete surface update variable $Y_h^n = X_h^n - X_h^{n-1}$, which is considered as unknown instead of the surface parametrization X^n . For time discretization, we again consider a semi-implicit Euler scheme following the strategy presented in Barrett *et al.* (2008) and Krause & Voigt (2023). We obtain the following discrete problem.

PROBLEM 3.2 (Discrete surface Navier–Stokes and surface update problem). *Find* $(u_h, p_h, \mathcal{H}_h, Y_h) \in [V_h \times V_h \times V_h \times V_h](\mathcal{S}_h^{n-1})$ such that

$$\left. \begin{aligned} \frac{1}{\tau} (u_h^n, v_h)_h + (\nabla_{w_h^{n-1}} u_h^n, v_h)_h &= (p_h^n, \operatorname{div}_P v_h)_h - \frac{2}{Re} ((\sigma(u_h^n), \nabla_P v_h)_h \\ &\quad + (\mu_h^n \nabla_S \phi_h^n, v_h)_h \\ &\quad + (\nabla_S(\kappa(\phi^n)(\mathcal{H}_h - \mathcal{H}_0(\phi^n))), \nabla_S(v_h \cdot v_h))_h \\ &\quad - (\kappa(\phi^n)(\mathcal{H}_h - \mathcal{H}_0(\phi^n))B^{n-1}, v_h \cdot v_h)_h \\ &\quad + \frac{1}{\tau} (u_h^{n-1}, v_h)_h - (\gamma u_h^n, v_h)_h, \\ (\operatorname{div}_P u_h^n, q_h)_h &= 0, \\ \frac{1}{\tau} (Y_h^n \cdot v_h, h_h)_h &= (u_h^n \cdot v_h, h_h)_h, \\ (\mathcal{H}_h^n v_h, Z_h)_h + (\kappa(\phi_h^n) \nabla_C Y_h^n, \nabla_C Z_h)_h &= -(\kappa(\phi_h^n) \nabla_C X_h^{n-1}, \nabla_C Z_h)_{\mathcal{H}} \end{aligned} \right\} \quad (3.11)$$

for all $(v_h, q_h, h_h, Z_h) \in [V_h \times V_h \times V_h \times V_h](\mathcal{S}_h^{n-1})$, where $B^{n-1} = (\|\mathcal{B}_h\|^2 - \frac{1}{2} \operatorname{tr} \mathcal{B}_h(\operatorname{tr} \mathcal{B}_h - \mathcal{H}_0(\phi^n)))$. (We note a typing error in Krause & Voigt (2023), which has been confirmed by the authors.)

The solutions of the discrete problems above are intermediate solutions with respect to the old surface \mathcal{S}_h^{n-1} . For each variable $\hat{\psi} \in V_h(\mathcal{S}_h^{n-1})$, we define the lift $\psi \in V_h(\mathcal{S}_h^n)$ by the evaluation with respect to the linear reference geometry where $\psi(X_h^n) = \hat{\psi}(X_h^{n-1})$. This corresponds to a nodal interpolation with respect to the degrees of freedom. We consider the following steps in each time step:

- (i) compute $(\hat{\phi}_h, \hat{\mu}_h) \in [V_h \times V_h](\mathcal{S}_h^{n-1})$ as intermediate solution of Problem 3.1;
- (ii) compute $(\hat{u}_h, \hat{p}, \hat{\mathcal{H}}_h, \hat{Y}_h) \in [V_h \times V_h \times V_h \times V_h](\mathcal{S}_h^{n-1})$ as intermediate solution of Problem 3.2;
- (iii) compute the new surface \mathcal{S}_h^n by updating its parametrization $X_h^n = X_h^{n-1} + Y_h^n$;
- (iv) lift the intermediate solutions on the new surface to get $(\phi_h, \mu_h) \in [V_h \times V_h](\mathcal{S}_h^n)$ and $(u_h, p, \mathcal{H}_h, Y_h) \in [V_h \times V_h \times V_h \times V_h](\mathcal{S}_h^n)$.

As numerical analysis results for the overall scheme are missing we justify the considered approach, essentially to perform just one iteration within each time step and the linearization of the nonlinear terms by comparing with an iterative Euler scheme. In this scheme we iterate Problems 3.1 and 3.2 within each time step until convergence and update all unknowns in each iteration. This can be considered as a fully implicit scheme. Similar fully implicit approaches for Navier–Stokes–Cahn–Hilliard equations have been considered in 2-D and 3-D settings, for example, Khanwale *et al.* (2020, 2023), and as the approaches mentioned above can be shown to be unconditionally energy stable. We compare the fully implicit iterative Euler scheme with our semi-implicit scheme for selected simulations, see Appendix E. The results are almost identical and indicate a reduction of computing time, which makes the following numerical studies to explore the complex interplay between surface phase composition, surface curvature and surface hydrodynamics feasible.

3.5. Implementational aspects

The discrete systems are implemented within the finite element toolbox AMDiS (Vey & Voigt 2007; Witkowski *et al.* 2015) based on DUNE (Alkämper *et al.* 2014; Sander 2020). The surface approximation is done by the Dune–CurvedGrid library developed in Praetorius & Stenger (2020). For a straightforward mesh parallelization and multiple processor computation we used the PETSc library and solved the linear system by using a direct solver. Due to the nature of the equations, which lack a maximum principle, we allow $\phi_h \in \mathbb{R}$ and extend all material parameters constantly for $\phi_h < -1$ and $\phi_h > 1$.

The SFEM approach discussed in § 3.2 does not support topological changes of the domain. Such changes can occur due to pinch offs associated with budding events or the formation of furrows. The pinch offs are characterized by a negative Gaussian curvature \mathcal{K} . We use this property as an indicator to define our simulated time interval $[0, T]$, where the final simulation time T is defined by $T = \inf\{t > 0 | \mathcal{K}(t) < \mathcal{K}_0\}$ where $\mathcal{K}_0 < 0$ is a chosen lower bound. If this criterion is not met, we consider $T = \infty$ and solve until an equilibrium configuration is reached. Numerical methods which are able to handle topological changes, or at least able to recover after such an event in a meaningful physical state, require an implicit description of the surface. Candidates are trace finite element methods (Jankuhn & Reusken 2020), cut finite element methods, level-set methods or diffuse interface methods (Nestler *et al.* 2018). However, these methods are computationally more expensive and currently not applicable for the considered problem. A comparison between SFEM and trace finite element methods for Stokes flow on stationary surfaces shows a factor of 10^2 – 10^3 lower errors for SFEM for comparable mesh sizes, depending on the considered error measure (Brandner *et al.* 2022a). Applications of cut finite element methods and level set methods for this problem class are not known and the first detailed numerical investigations for diffuse interface methods for vector-valued surface PDEs show strong limitations for the required accuracy for the reconstructed geometric terms (Nestler & Voigt 2023a). These results are supported in a benchmark problem for vector-valued diffusion on surfaces with large curvature (Bachini *et al.* 2023a). This motivates the use of SFEM and the needs to consider simulations only before a potential topological change.

4. Numerical results

4.1. Considered parameters and initial conditions

Let \mathcal{S} be the unit sphere with radius $R = 1$. The velocity field is initialized by $\mathbf{u}_0 = 0$ and we define two different initial configurations for the phase field. The first one is

$\phi_0(\mathbf{x}) = \tanh(x_0/\sqrt{2})$ that defines a symmetric and equal distributed phase field where the phases are separated. The second one defines a random initial condition: $\phi_1 = \min\{\max\{\hat{\phi}_1, -1\}, 1\}$, where $\hat{\phi}$ is given by Gaussian random field,

$$\hat{\phi}_1(\mathbf{x}) = -1.0 + \sum_{i=0}^N \exp\left(-\frac{\beta}{2}\|\mathbf{x} - \mathbf{x}_i\|^2\right) \quad \forall \mathbf{x} \in \mathcal{S}, \tag{4.1}$$

where $\{\mathbf{x}_i\}_0^N \subset \mathcal{S}$ and $\beta = 100$. This allows us to create a reproducible random initial condition. Both configurations consider an equal distributed phase field. We vary the Reynolds number Re and the bending stiffness κ but set $\mathcal{H}_0 = \gamma = 0$. Other parameters are set to $\epsilon = 0.02$, $m = 0.001$ and $\sigma = 1.0$ ($\tilde{\sigma} = \frac{3}{2}\sqrt{2}$), which provides a good compromise between computational effort and physical accuracy. Numerical parameters are such that $h^3 \sim \tau$. This relation results from the properties of the discretization scheme, which can be expected to be first order in time and third order in space, which will be computationally confirmed below.

4.2. Convergence study

Due to the tight coupling between the phase field ϕ , the surface velocity \mathbf{u} , the surface pressure p and the geometry \mathcal{S} we expect the numerical solution to sensitively depend on the approximations. Therefore, we start by considering a convergence study. Due to a lack of analytical solutions for the full problem, we compute a numerical solution with a fine discretization and study convergence with respect to this solution. In addition, we address general properties of the solution.

We compute the errors with respect to the L^2 norm in space and the L^∞ norm in time. The norms are calculated with respect to the linear reference geometry \mathcal{S}_h^{lin} , where the evaluation of the norms on different surfaces $\mathcal{S}, \mathcal{S}_h, \mathcal{S}_h^{lin}$ leads to equivalent norms with the same order of convergence (Demlow 2009). We define the following errors:

$$\left. \begin{aligned} e_X &= \|\mathbf{X}_h - \mathbf{X}\|_{L^\infty(L^2(\mathcal{S}_h^{lin}))}, \\ e_u &= \|\mathbf{u}_h(\mathbf{X}_h) - \mathbf{u}(\mathbf{X})\|_{L^\infty(L^2(\mathcal{S}_h^{lin}))}, \\ e_\phi &= \|\phi_h(\mathbf{X}_h) - \phi(\mathbf{X})\|_{L^\infty(L^2(\mathcal{S}_h^{lin}))}, \\ e_A &= \|\mathcal{S}_h(t) - \mathcal{S}_h(0)\|_{L^\infty}, \\ e_{divp} &= \|\text{divp}\mathbf{u}_h\|_{L^\infty(L^2(\mathcal{S}_h))}, \\ e_{\mathcal{F}} &= |(\mathcal{F}_{K_h} + \mathcal{F}_h) - (\mathcal{F}_K + \mathcal{F})|_{L^\infty}, \end{aligned} \right\} \tag{4.2}$$

with discrete solutions $\mathbf{X}_h, \mathbf{u}_h, \phi_h$ with varying h and $\mathbf{X}, \mathbf{u}, \phi$ the discrete reference solutions with the finest mesh size. Additionally, we measure the area conservation error e_A , the local inextensibility error e_{divp} and the error of the total energy $e_{\mathcal{F}}$, where again \mathcal{F}_K and \mathcal{F} denote the discrete reference solution on the finest mesh size. The simulations are done for the random initial condition ϕ_1 with $Re = 1.0$ and $\kappa_1 = \kappa_2 = \kappa = 0.02$.

The results are shown in figure 1. They indicate third-order convergence for the surface error e_X and the error of the phase field e_ϕ , which corresponds to the results in Praetorius & Stenger (2020) and Demlow (2009) for simple mean curvature flow and scalar-valued surface PDEs. The order of convergence for the phase field e_ϕ also agrees with the one obtained for the corresponding problem on stationary surfaces considered in Bachini et al. (2023b). For the error of the velocity field e_u the results indicate second-order

A two-phase fluid deformable surface model

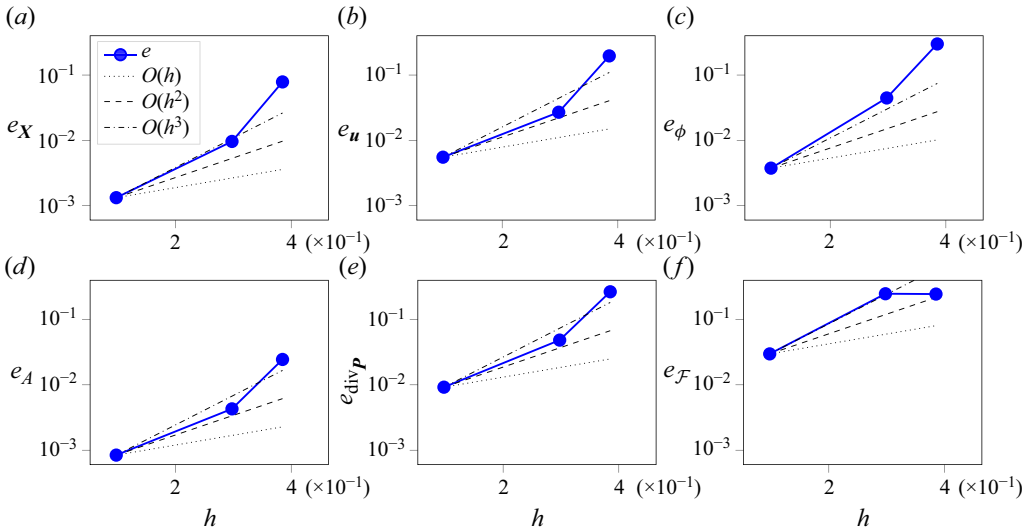


Figure 1. Convergence study for two-phase fluid deformable surfaces with respect to the mesh size $h^3 \sim \tau$ for X_h , u_h , ϕ_h (a–c); and error for area A , divergence $\text{div}P u_h$ and total energy $\mathcal{F}_K + \mathcal{F}$ (d–f).

convergence in accordance with the results in Krause & Voigt (2023) for one-component fluid deformable surfaces. In Brandner *et al.* (2022a), third-order convergence of e_u is shown for the tangential flow of the surface Stokes equations on stationary surfaces. However, this requires a higher-order approximation of the normal vector (Hansbo *et al.* 2020; Hardering & Praetorius 2022), which is not fulfilled in our approach. Furthermore, it remains open if this increased order also emerges for the surface Navier–Stokes equations and on evolving surfaces. For the area conservation error e_A and the inextensibility error $e_{\text{div}P}$ we get second-order convergence with respect to h . Both are related to each other. While $e_A = 0$, the same order for $e_{\text{div}P}$ has been obtained in Bachini *et al.* (2023b) for a stationary surface. The convergence error of the total energy indicates third order. This might be due to the dominating effect of Ginzburg–Landau energy as the expected order for the underlying Helfrich model would be lower (Dziuk 2008). However, overall we see experimentally the expected optimal order of convergence for the full problem.

4.3. Phase separation, bulging and induced flow

To demonstrate the strong interplay between composition, curvature and hydrodynamics we consider ϕ_1 as an initial condition. The other parameters are $Re = 1.0$ and either $\kappa_1 = \kappa_2 = \kappa = 0.02$ or $\kappa_1 = 0.02$ and $\kappa_2 = 0.5$. In the last case, the red coloured phase has a lower bending stiffness and is therefore expected to be guided or initiate regions with higher mean curvature, while the blue coloured phase has a larger bending stiffness and can be expected to prefer regions of lower mean curvature. The evolution is shown in figure 2(a,b), respectively. Both cases show the composition and the tangential velocity for selected time instances. In both cases red and blue islands form and a wavy interface between larger red and blue regions is established. Some coarsening events can be spotted and the wavy interface flattens over time. However, the main evolution is in the shape, which strongly deforms and forms bulges. Especially for circular islands the interface length is reduced by bulging leading to strong deformation from the sphere. These shapes

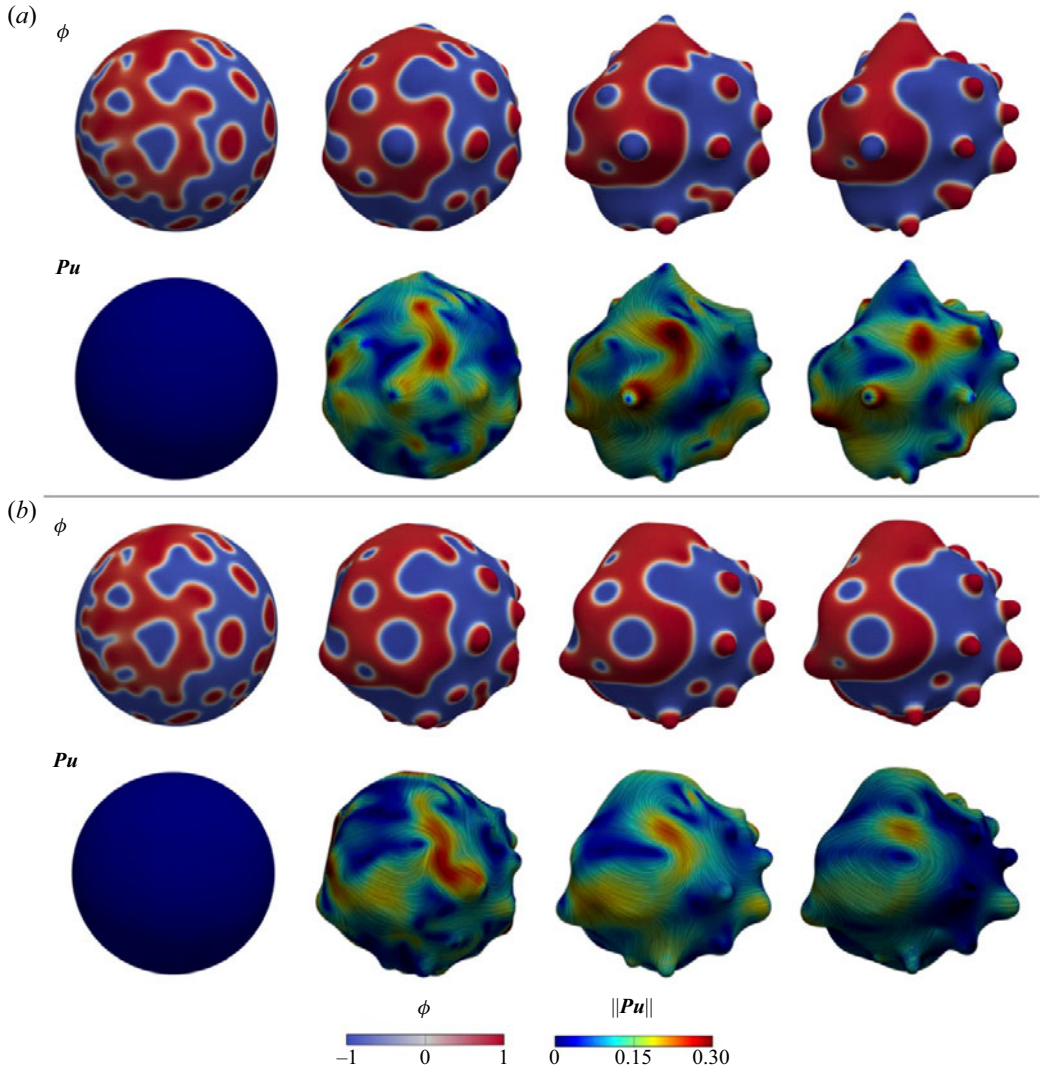


Figure 2. (a,b) Snapshots of the relaxation of the two-component fluid deformable surface with random initial condition ϕ_1 and $Re = 1.0$ for $t = 0, 0.3, 0.8, 1.1$ (from left to right), with constant bending stiffness $\kappa_1 = \kappa_2 = \kappa = 0.02$ in (a) and phase-dependent bending stiffness $\kappa_1 = 0.02$ and $\kappa_2 = 0.5$ in (b). In (b) the red coloured phase is less stiff than the blue coloured phase. Here, in each of (a,b), is shown the (top) phase field ϕ ; (bottom) tangential velocity Pu . The flow is visualized by a LIC (Line Integral Convolution) filter and colour coding represents the magnitude. Corresponding movies are provided in the Supplementary data available at <https://doi.org/10.1017/jfm.2023.943>.

change, but also the coarsening events induce flow. The simulations are only shown for a relatively short period of time and are terminated before a potential topological change would happen. Differences between figure 2(a) and figure 2(b) are also visible. While in figure 2(a) the red and blue phases evolve similarly, in figure 2(b) the blue phase, the one associated with a larger bending stiffness, forms less curved regions. Especially, islands of this phase do not bulge out. Instead, they become relatively flat. The behaviour of the simulation shown in figure 2 is quantified in figure 3 by different energies. In the current setting, the evolution is dominated by \mathcal{F}_{GL} , which is reduced by coarsening but also by

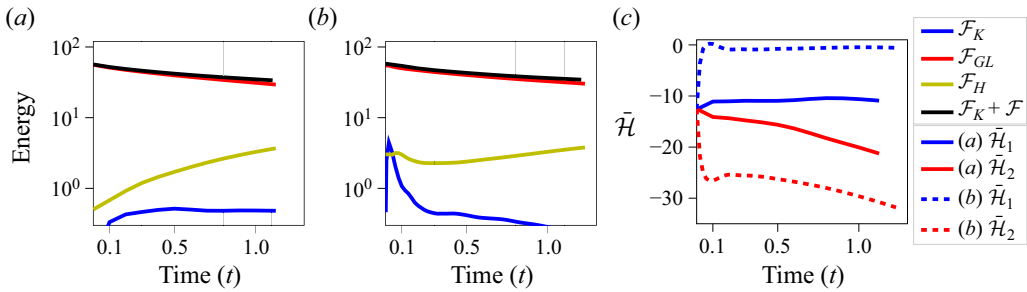


Figure 3. (a,b) The energies \mathcal{F}_K , \mathcal{F}_{GL} , \mathcal{F}_H and $\mathcal{F}_K + \mathcal{F}$ over time where (a) corresponds to figure 2(a) and (b) corresponds to figure 2(b). The time instances are highlighted in the plots. (c) Averaged mean curvature $\bar{\mathcal{H}}_{1,2}$ for the different phases with respect to the simulations done in figure 2(a,b), the colour corresponds to the coloured phases.

bulging, which is associated with an increase in \mathcal{F}_H . Hydrodynamics seems to play a minor role in the evolution. Here \mathcal{F}_K is one to two orders of magnitude lower than \mathcal{F}_{GL} . The strong increase of \mathcal{F}_K and \mathcal{F}_H at the beginning is associated with the increased driving force resulting from the phase-dependent bending stiffness. The spatial average over the mean curvature for the red and the blue phase, i.e.

$$\bar{\mathcal{H}}_1 = \int_{\{\phi < 0\}} \mathcal{H} \quad \text{and} \quad \bar{\mathcal{H}}_2 = \int_{\{\phi > 0\}} \mathcal{H}, \quad (4.3a,b)$$

is shown in figure 3(c). The deviation between $\bar{\mathcal{H}}_1$ and $\bar{\mathcal{H}}_2$ for the setting of figure 2(a) results from asymmetries in the initial condition. For the setting of figure 2(b), these quantities show strong differences between the different phases. The blue phase on average forms flat regions, while the red phase forms strongly curved bulges.

4.4. Variation of parameters

We now explore the influence of the parameters in more detail. To reduce the number of parameters we only consider the situation of a constant bending stiffness $\kappa_1 = \kappa_2 = \kappa$, set $\kappa = \{0.02, 0.1, 0.5\}$, and vary the Reynolds number with $Re = \{0.1, 1, 3\}$. We consider both initial conditions ϕ_0 and ϕ_1 . The behaviour is demonstrated for the symmetric initial phase field ϕ_0 in figure 4 and for the random initial phase field ϕ_1 in figure 5. We only show the final configuration, this is either the equilibrium configuration or the configuration at the critical time T before a potential pinch-off. A table with critical final times is presented in table 1. In the first case (ϕ_0) the final configuration is mainly determined by the interplay of the Helfrich energy \mathcal{F}_H and the Ginsburg–Landau energy \mathcal{F}_{GL} . For $\kappa = 0.5$, \mathcal{F}_H dominates. Any deformation of the initial sphere requires us to increase the Helfrich energy. Only small deformations are possible. The interface length, and thus \mathcal{F}_{GL} , is reduced by deforming the sphere to an ellipsoid-like shape with the interface placed along the short axis. Further reduction of the interface length either requires to increase the mean curvature at the tips of the long axis of this shape or to form a furrow along the interface. Both effects strongly increase \mathcal{F}_H . This is only realized for settings with lower κ and eventually will lead to a pinch-off. Hydrodynamics seems to have no significant effect in these evolutions. However, a closer look at the consider critical times T in table 1 shows the opposite. While the final configurations look similar, the time to reach these configurations is strongly influenced by hydrodynamics. For low bending

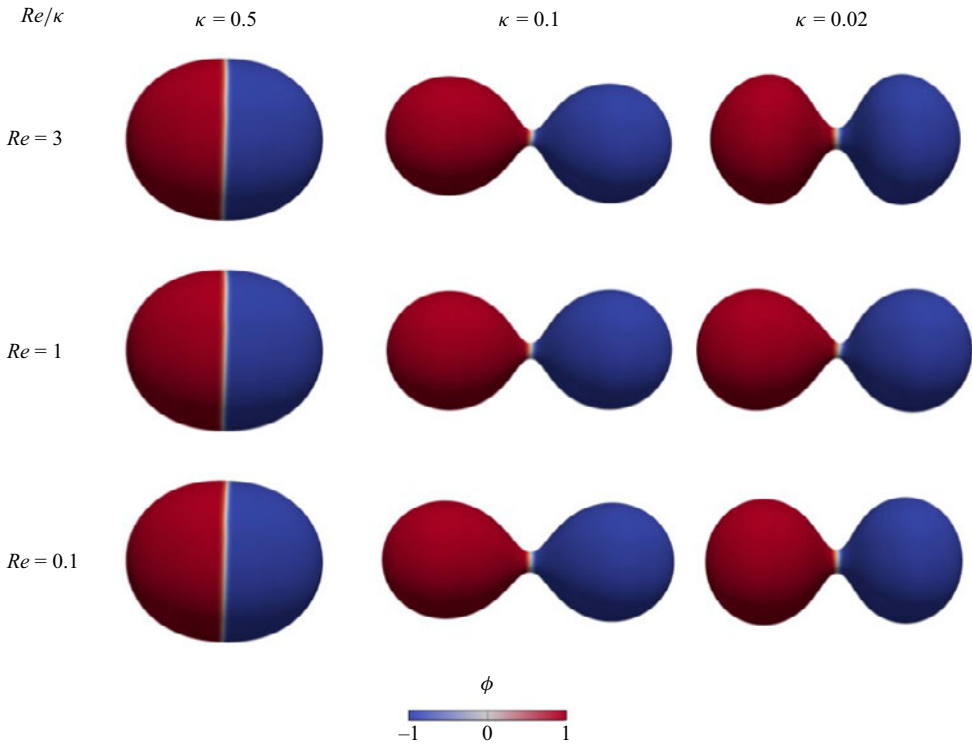


Figure 4. Final configuration obtained for different parameters and initial condition ϕ_0 . Either the simulation reaches the equilibrium configuration or the criteria for a potential pinch-off is reached. The corresponding critical times T are shown in [table 1](#).

stiffness, $\kappa = \{0.1, 0.02\}$, the critical time is drastically reduced if the Reynolds number Re is increased.

For the random initial condition ϕ_1 the results are shown in [figure 5](#). Here, we have an interplay between coarsening, shape deformation, bulging and furrow formation. For large bending stiffness $\kappa = 0.5$, where strong shape deformations are suppressed, the same final configuration as in [figure 4](#) is reached, meaning an ellipsoidal-like shape with the interface placed along the short axis. This changes for lower κ . For $\kappa = 0.1$, we observe partial coarsening, bulging of islands and the formation of a furrow, which eventually leads to a pinch-off. The configurations also change with hydrodynamics. For $Re = 3$ the potential pinch-off happens earlier. Several islands are still present in the red as well as the blue phase. Decreasing Re also leads to possible pinch-offs but at a later coarsening state. There are fewer islands present. While it is known in flat space that hydrodynamics can enhance coarsening and this is also demonstrated on stationary surfaces (Bachini *et al.* [2023b](#)), these results indicate that this also holds on evolving surfaces and that hydrodynamics enhances furrow formation and potential pinch-off. This is confirmed in [table 1](#), which again shows a drastic reduction of the critical time T . For $\kappa = 0.02$ the evolution is dominated by bulging. As discussed in the previous section bulging is associated with large local absolute mean curvature values but allows us to reduce the interface length. The critical time results from potential pinch-offs of the bulges. Coarsening is only a minor effect. Again hydrodynamic drastically enhances the evolution. Increasing Re again drastically reduces the time for potential pinch-off, see [table 1](#).

A two-phase fluid deformable surface model

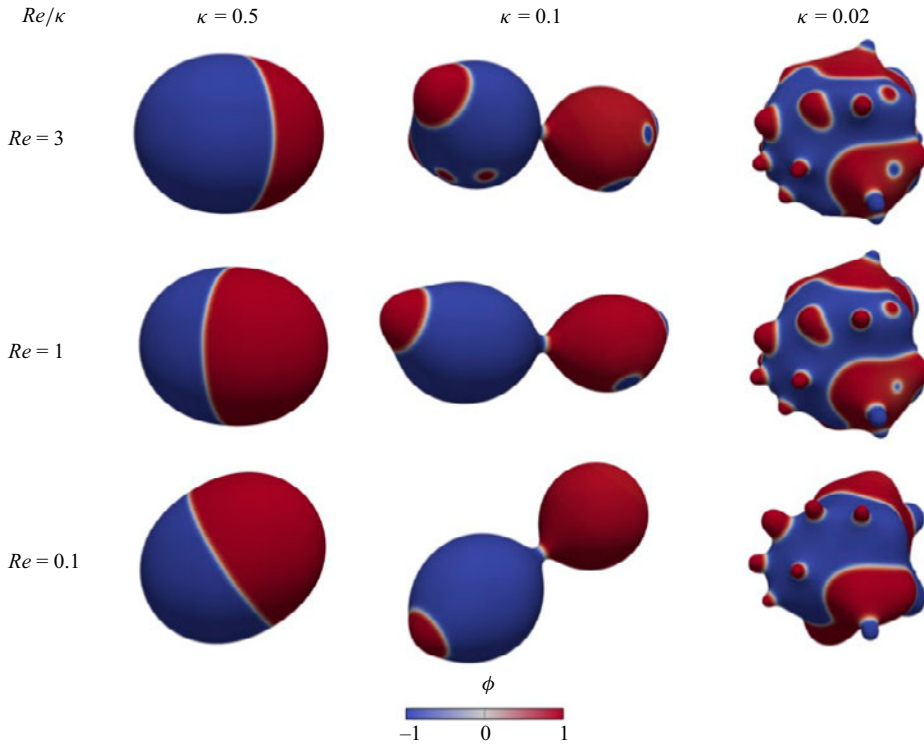


Figure 5. Final configuration obtained for different parameters and initial condition ϕ_1 . Either the simulation reaches the equilibrium configuration or the criteria for a potential pinch-off is reached. The corresponding critical times T are shown in table 1.

(a)	Re/κ	0.5	0.1	0.02	(b)	Re/κ	0.5	0.1	0.02
	3	∞	5.6	1.9		3	∞	9.1	0.5
	1	∞	10.7	5.3		1	∞	20.0	1.1
	0.1	∞	87.0	42.0		0.1	∞	170.5	9.8

Table 1. Critical times T for the different Reynolds numbers Re and bending stiffness κ for the symmetric initial value ϕ_0 in (a) and the random initial value ϕ_1 in (b).

We also would like to comment on the axisymmetric ellipsoidal-like configurations reached for $\kappa = 0.5$. With friction $\gamma > 0$ these configurations would be characterized by zero tangential velocity $\mathbf{P}\mathbf{u} = 0$ and they would be independent on the initial condition and the Reynolds number Re . This equilibrium state coincides with the corresponding result for the reduced model without hydrodynamics, see Appendix D. However, without friction $\gamma = 0$ the dissipation potential in the reached axisymmetric state is invariant under surface rigid body motion. Such configurations have been explored for one-component fluid deformable surfaces (Reuther *et al.* 2020; Krause & Voigt 2023; Nestler & Voigt 2023b; Olshanskii 2023). Indeed the shown configurations in figures 4 and 5 for $\kappa = 0.5$ undergo slight rigid body motions and as the resulting forces interact with the shape and the phase composition also slightly differ. This result can be viewed as an extension of the phenomenon of rotating equilibrium states from one-component to two-component fluid deformable surfaces. However, as discussed in Nestler & Voigt (2023b) any perturbation

in shape or velocity that destroys the axisymmetric configurations leads to dissipation and we therefore can expect for $t \rightarrow \infty$ to reach the mentioned equilibrium state with $\mathbf{P}\mathbf{u} = 0$.

However, the main focus of this paper is on the dynamics. One could ask about the behaviour if the Reynolds number Re is further reduced. This can be considered in the Stokes limit. This limit cannot be directly derived by the Lagrange–d’Alembert principle and requires some further thoughts on the fluid–solid duality of the fluid deformable surface model, which will be explored in future research. However, we can already remark that the dynamics for two-phase fluid deformable surfaces, also for low Re , strongly differ from previous models neglecting surface viscosity. The derivation by the Lagrange–d’Alembert principle accounts for normal and tangential variations, which differs from various previous approaches, see, for example, Elliott & Stinner (2010a). Qualitative differences already result from the tangential flow induced by the phase boundary, see Appendix D for corresponding results of the model proposed in Elliott & Stinner (2010a) with additional local inextensibility constraint. These differences are further enhanced by hydrodynamics.

5. Conclusions

While the literature on coexisting fluid domains in model systems for biomembranes and their dynamics is rich, the influence of surface viscosity has not been discussed in this context. We have filled this gap and derived a thermodynamically consistent model that accounts for surface hydrodynamics. The derivation of the model by a Lagrange–d’Alembert principle is applicable in general. Simplifications of the derived two-phase fluid deformable surface model lead to known models in the literature, and this further confirms the validity of the approach.

By combining numerical approaches for fluid deformable surfaces (Krause & Voigt 2023) and two-phase flow models on stationary surfaces (Bachini *et al.* 2023b), we obtain a numerical approach for the full model, which is demonstrated to converge with expected optimal order. This provides the basis for a detailed investigation of the strong interplay of surface phase composition, surface curvature and surface hydrodynamics. Depending on the material parameters, the line tension σ , the Reynolds number Re and the bending stiffness κ , the evolution is dominated by coarsening or shape evolution. Both phenomena are shown to be strongly enhanced by hydrodynamics. In situations where the line tension and the bending stiffness are compatible, the interface length is reduced by the formation of a furrow or the formation of bulges. Both potentially lead to pinch-offs. The enhanced evolution towards such topological changes driven by hydrodynamics has various biological implications. In the context of a furrow formation and its subsequent shrinkage, this can be associated with cell division (Mietke *et al.* 2019); in the context of bulges with pinch-offs, this can be associated with endocytosis and exocytosis (Kaksonen & Roux 2018; Al-Izzi *et al.* 2020). While quantitative comparisons with experimental data in these contexts require further studies, the mathematical model and the numerical algorithm to solve it with the required accuracy are provided.

Supplementary movies. Supplementary movies are available at <https://doi.org/10.1017/jfm.2023.943>.

Acknowledgements. We acknowledge computing resources provided by ZIH at TU Dresden and by JSC at FZ Jülich, within projects WIR and PFAMDIS, respectively.

Funding. This work was supported by the German Research Foundation (DFG) within the Research Unit ‘Vector- and Tensor-Valued Surface PDEs’ (FOR 3013).

Declaration of interests. The authors report no conflict of interest.

Data availability statement. The data that support the findings of this study are available from the corresponding author upon reasonable request.

Author ORCIDs.

 Elena Bachini <https://orcid.org/0000-0001-8610-9426>;

 Axel Voigt <https://orcid.org/0000-0003-2564-3697>.

Appendix A. Symbols, definitions and geometric notation

We define the surface differential operators as used in § 2, pointing out the differences if they are applied to scalar, vector or tensor quantities.

A.1. Scalar fields

Let $f \in T^0\mathcal{S}$ be a scalar field with arbitrary smooth extension f^e , i.e. $f^e|_{\mathcal{S}} = f$. The componentwise, tangential or covariant derivative is given by

$$\nabla_C f = \nabla_P f = \nabla_S f = (P^e \nabla f^e)|_{\mathcal{S}} = P(\nabla f^e)|_{\mathcal{S}}. \quad (A1)$$

An alternative definition of the same operators without considering the extension f^e is given by

$$\nabla_C f = \nabla_P f = \nabla_S f = g^{ij} \partial_j f \partial_i X = (g^{ij} \partial_j f \partial_i X^A) e_A, \quad (A2)$$

where g^{ij} are the contravariant/inverse components of the metric tensor on \mathcal{S} obtained by a parametrization X .

A.2. Vector fields

Let $u = u_T + u_N v \in T\mathbb{R}^3|_{\mathcal{S}}$ be a vector field with arbitrary smooth extension u^e , i.e. $u^e|_{\mathcal{S}} = u$. We define the componentwise and tangential derivatives, respectively, by

$$\nabla_C u = ((P^e \nabla) u^e)|_{\mathcal{S}} = (\nabla u^e)|_{\mathcal{S}} P \quad (\text{componentwise derivative}), \quad (A3)$$

$$\nabla_P u = (P^e (\nabla u^e) P^e)|_{\mathcal{S}} = P(\nabla u^e)|_{\mathcal{S}} P \quad (\text{tangential derivative}). \quad (A4)$$

A covariant derivative is uniquely defined for pure tangential vector fields (i.e. $u_N = 0$) by

$$\nabla_S u_T = g^{jk} (\partial_k u_T^i + \Gamma_{kl}^i u_T^l) \partial_i X \otimes \partial_j X, \quad (A5)$$

where $\Gamma_{\cdot\cdot}^{\cdot}$ are the Christoffel symbols determined by the metric tensor. The relation to the tangential and componentwise derivatives is given by

$$\nabla_P u = g^{ik} g^{jl} (\partial_l u, \partial_k X) \partial_i X \otimes \partial_j X = P \nabla_C u = \nabla_S u_T - u_N \mathcal{B}, \quad (A6)$$

$$\nabla_C u = e_A \otimes \nabla_S u^A = g^{ij} (\partial_j u) \otimes \partial_i X = \nabla_S u_T - u_N \mathcal{B} + v \otimes (\nabla_S u_N + \mathcal{B} u_T). \quad (A7)$$

By definition, the covariant and tangential derivatives of vector fields are purely tangential operators but the componentwise derivative contains normal components too. We define the corresponding divergence operators by

$$\text{div}_S u_T = \text{tr } \nabla_S u_T = \partial_i u_T^i + \Gamma_{ik}^i u_T^k, \quad (A8)$$

$$\text{div}_C u = \text{div}_P u = \text{tr } \nabla_C u = \text{tr } \nabla_P u = \text{div}_S u_T - u_N \mathcal{H}. \quad (A9)$$

A.3. Tensor fields

Let $\sigma \in T^2\mathbb{R}^3|_S$ be a tensor field with arbitrary smooth extension σ^e , i.e. $\sigma^e|_S = \sigma$. The definition of the componentwise, tangential or covariant derivative is possible for arbitrary tensor fields but we will show only the definitions of the operators used in this paper. To do so, we define the componentwise derivative by

$$\nabla_C \sigma = ((P^e \nabla) \sigma^e)|_S = (\nabla \sigma^e)|_S P \tag{A10}$$

$$= e_A \otimes e_B \otimes \nabla_S \sigma^{AB} = g^{ij} (\partial_j \sigma) \otimes \partial_i X. \tag{A11}$$

The covariant divergence for the pure tangential tensor field $\epsilon = P\sigma P \in T^2S$ is defined by

$$\text{div}_S \epsilon = (\partial_j \epsilon^{ij} + \Gamma_{jk}^i \epsilon^{kj} + \Gamma_{jk}^j \epsilon^{ik}) \partial_i X. \tag{A12}$$

We define a componentwise divergence for right side tangential tensor field σP by

$$\begin{aligned} \text{div}_C(\sigma P) &= \text{tr } \nabla_C(\sigma P) = (e_B, \nabla_S[\sigma P]^{AB}) e_A \\ &= \text{div}_S(P\sigma P) - \nu \sigma \mathcal{B} + ((\sigma, \mathcal{B}) + \text{div}_S(\nu \sigma P)) \nu. \end{aligned} \tag{A13}$$

The reason for defining only this restricted version of the componentwise divergence is that $\text{tr} \circ \nabla_C$ would not be the adjoint operator of ∇_C and thus the integration by parts formula (A15) would no longer hold in general.

A.4. Integration by parts formulae

An integration by parts formulae can be derived for the differential operators above. The following uses the global inner product neglecting the boundary terms. For all tangential tensor fields $\epsilon = P\sigma P \in T^2S$ and vectors fields $u \in T\mathbb{R}^3|_S$, the following relations hold:

$$(\sigma, \nabla_P u) = (\epsilon, \nabla_P u) = (\epsilon, \nabla_C u) = -(\text{div}_C \epsilon, u), \tag{A14}$$

$$(\sigma P, \nabla_C u) = -(\text{div}_C(\sigma P), u). \tag{A15}$$

These relations follow from (A7) and (A13). For all $f \in T^0S$ and $u \in T\mathbb{R}^3|_S$, we have

$$(f, \text{div}_P u) = (f, \text{div}_C u) = -(\text{div}_C(fP), u) = -(\nabla_S f + f \mathcal{H} \nu, u), \tag{A16}$$

which follows from (A14), (A1), (A13) and metric compatibility $\nabla_S P = 0$.

A.5. Laplace operators

For scalar fields, we define a Laplace operator by the Laplace–Beltrami operator Δ_S ,

$$\Delta_S f = \text{div}_S \nabla_S f = \text{div}_P \nabla_P f = \text{div}_C \nabla_C f = g^{ij} (\partial_i \partial_j f - \Gamma_{ij}^k \partial_k f), \tag{A17}$$

and the componentwise Laplace operator for vector fields $u = u^A e_A$ by

$$\Delta_C u = \text{div}_C \nabla_C u = (\Delta_S u^A) e_A, \tag{A18}$$

where u^A are the Cartesian components with respect to the Cartesian basis vectors e_A .

Appendix B. The Lagrange–d’Alembert principle for the full model

B.1. General procedure

For state variables X (parametrization of \mathcal{S}) and $\phi \in T^0\mathcal{S}$ (phase field), and process variables $\mathbf{u} \in T\mathbb{R}^3|_{\mathcal{S}}$ (material velocity) and $\dot{\phi} \in T^0\mathcal{S}$ (phase field rate), the Lagrange–d’Alembert principle generally reads (see Marsden & Ratiu (2013))

$$\left(\frac{\delta\mathcal{A}}{\delta X}, \mathbf{Y}\right) + \left(\frac{\delta\mathcal{A}}{\delta\phi}, \psi\right) = \int_{t_0}^{t_1} \left(\frac{\delta\mathcal{D}}{\delta\mathbf{u}}, \mathbf{Y}\right) + \left(\frac{\delta\mathcal{D}}{\delta\dot{\phi}}, \psi\right) \quad \forall \mathbf{Y} \in T\mathbb{R}^3|_{\mathcal{S}}, \quad \psi \in T^0\mathcal{S}, \tag{B1}$$

where \mathcal{D} is the dissipation potential and $\mathcal{A} = \int_{t_0}^{t_1} \mathcal{L}$ is the action functional, in which the Lagrangian is defined by $\mathcal{L} = \mathcal{F}_K - \mathcal{F}$, with kinetic energy $\mathcal{F}_K = \int_{\mathcal{S}}(\rho/2) \|\mathbf{u}\|^2$, potential energy \mathcal{F} and time interval $[t_0, t_1]$.

In a first step, we localize (B1) in time. Assuming that the potential energy \mathcal{F} depends only on state variables, we only have to consider the kinetic energy \mathcal{F}_K for this purpose. Note that time integration commutes with spatial variations in a non-relativistic setting. For instance, the following holds $((\delta/\delta X) \int_{t_0}^{t_1} \mathcal{F}_K, \mathbf{Y}) = \int_{t_0}^{t_1} (\delta\mathcal{F}_K/\delta X, \mathbf{Y})$. In contrast, spatial integration does clearly not commute with spatial variation. From Nitschke *et al.* (2022), we adopt the identity

$$\left(\frac{\delta}{\delta X} \int_{\mathcal{S}} f, \mathbf{Y}\right) = \int_{\mathcal{S}} \bar{\partial}_Y f + f \operatorname{div}_P \mathbf{Y} \quad \forall f \in T^0\mathcal{S}, \quad \mathbf{Y} \in T\mathbb{R}^3|_{\mathcal{S}}, \tag{B2}$$

where $\bar{\partial}_Y : T^0\mathcal{S} \rightarrow T^0\mathcal{S}$ is the deformation derivative in direction of \mathbf{Y} , i.e.

$$\bar{\partial}_Y f := \left. \frac{d}{d\varepsilon} \right|_{\varepsilon=0} (f|_{X+\varepsilon Y}) \quad \forall f \in T^0\mathcal{S}, \quad \mathbf{Y} \in T\mathbb{R}^3|_{\mathcal{S}}. \tag{B3}$$

We assume a variational mass conservation, i.e.

$$0 = \left(\frac{\delta}{\delta X} \int_U \rho, \mathbf{Y}\right) = \int_U \bar{\partial}_Y \rho + \rho \operatorname{div}_P \mathbf{Y} \quad \forall U \subseteq \mathcal{S}, \quad \mathbf{Y} \in T\mathbb{R}^3|_{\mathcal{S}}, \tag{B4}$$

valid for mass density $\rho \in T^0\mathcal{S}$. Since the subset $U \subseteq \mathcal{S}$ is arbitrary, $\bar{\partial}_Y \rho = -\rho \operatorname{div}_P \mathbf{Y}$ holds locally. In addition, we assume temporal mass conservation, $\dot{\rho} = -\rho \operatorname{div}_P \mathbf{u}$, and vanishing variation directions at times t_0 and t_1 , i.e. $\mathbf{Y}|_{t_0} = \mathbf{Y}|_{t_1} = 0$. The fundamental theorem of calculus, temporal integration by parts, transport formula and $\bar{\partial}_Y \mathbf{u} = \dot{\mathbf{Y}}$ Cartesian-componentwise together yields

$$\begin{aligned} \left(\frac{\delta}{\delta X} \int_{t_0}^{t_1} \mathcal{F}_K, \mathbf{Y}\right) &= \int_{t_0}^{t_1} \left(\frac{\delta\mathcal{F}_K}{\delta X}, \mathbf{Y}\right) = \int_{t_0}^{t_1} (\rho\mathbf{u}, \dot{\mathbf{Y}}) + \int_{\mathcal{S}} \frac{\|\mathbf{u}\|^2}{2} (\bar{\partial}_Y \rho + \rho \operatorname{div}_P \mathbf{Y}) \\ &= \int_{t_0}^{t_1} \frac{d}{dt} (\rho\mathbf{u}, \mathbf{Y}) - (\rho\dot{\mathbf{u}}, \mathbf{Y}) - \frac{1}{2} \int_{\mathcal{S}} (\dot{\rho} + \rho \operatorname{div}_P \mathbf{u}) (\mathbf{u}, \mathbf{Y}) \\ &= - \int_{t_0}^{t_1} (\rho\dot{\mathbf{u}}, \mathbf{Y}). \end{aligned} \tag{B5}$$

Finally, the temporal localized version of the Lagrange–d’Alembert principle (B1) reads

$$0 = (\rho\dot{\mathbf{u}} + \mathbf{D}_X \mathcal{F} + \mathbf{D}_u \mathcal{D}, \mathbf{Y}) + (\mathbf{D}_\phi \mathcal{F} + \mathbf{D}_\phi \mathcal{D}, \psi) \quad \forall \mathbf{Y} \in T\mathbb{R}^3|_{\mathcal{S}}, \quad \psi \in T^0\mathcal{S}, \tag{B6}$$

where the negative generalized applied forces $\mathbf{D}_X \mathcal{F}, \mathbf{D}_u \mathcal{D} \in T\mathbb{R}^3|_{\mathcal{S}}$ and $\mathbf{D}_\phi \mathcal{F}, \mathbf{D}_\phi \mathcal{D} \in T^0\mathcal{S}$ are given as L^2 -gradients, i.e. $(\mathbf{D}_X \mathcal{F}, \mathbf{Y}) = (\delta\mathcal{F}/\delta X, \mathbf{Y})$ and $(\mathbf{D}_u \mathcal{D}, \mathbf{Y}) =$

$(\delta\mathcal{D}/\delta\mathbf{u}, \mathbf{Y})$ for all virtual displacements $\mathbf{Y} \in T\mathbb{R}^3|_S$, as well as $(\mathbf{D}_\phi\mathcal{F}, \psi) = (\delta\mathcal{F}/\delta\phi, \psi)$ and $(\mathbf{D}_\dot{\phi}\mathcal{D}, \psi) = (\delta\mathcal{D}/\delta\dot{\phi}, \psi)$ for all virtual displacements $\psi \in T^0\mathcal{S}$.

Next, in § B.2, we calculate the negative Lagrangian forces $\mathbf{D}_X\mathcal{F}$ and $\mathbf{D}_\phi\mathcal{F}$, and the negative dissipative forces $\mathbf{D}_u\mathcal{D}$ and $\mathbf{D}_\dot{\phi}\mathcal{D}$ in § B.3, according to the potential energy \mathcal{F} and the dissipation potential \mathcal{D} given in this paper. Moreover, we implement local inextensibility of the material by the Lagrange-multiplier technique in § B.4. Eventually, the strong formulation of (B6) and a tangential-normal splitting of the Lagrangian force to $\mathbf{b}_T := -\mathbf{P}\mathbf{D}_X\mathcal{F}$ and $\mathbf{b}_N := -(\mathbf{v}, \mathbf{D}_X\mathcal{F})\mathbf{v}$ leads to the full model given in Problem 2.1. Note that, in our derivations, we assume *a priori* independence between the phase field ϕ and the surface given by the parametrization X . Therefore, $\delta_Y\phi = 0$ is valid for all $\mathbf{Y} \in T\mathbb{R}^3|_S$ (see Nitschke *et al.* (2022) for more details), where this *a priori* condition is referred to the scalar gauge of surface independence. In contrast to L^2 -gradient flow techniques, here this assumption is not necessary to determine (B6), since all terms containing $\delta_Y\phi$ would vanish anyway. However, taken the generalized applied forces individually would comprises terms of the undetermined quantity $\delta_Y\phi$ in a weak sense. Consequently, we would have to choose $\delta_Y\phi = 0$ to give these forces a determined meaning.

B.2. Lagrangian forces

In this section we consider the potential energy $\mathcal{F} = \mathcal{F}_{GL} + \mathcal{F}_H$, which is composed by the Ginzburg–Landau energy $\mathcal{F}_{GL} = \tilde{\sigma} \int_S (\epsilon/2) \|\nabla_S\phi\|^2 + (1/\epsilon)W(\phi)$ (2.3) and the Helfrich energy $\mathcal{F}_H = \int_S \frac{1}{2}\kappa(\phi)(\mathcal{H} - \mathcal{H}_0(\phi))^2$ (2.4). Without much mathematical effort, computing the negative generalized applied forces $\mathbf{D}_\phi\mathcal{F}_{GL}, \mathbf{D}_\phi\mathcal{F}_H \in T^0\mathcal{S}$ gives

$$\left. \begin{aligned} \mathbf{D}_\phi\mathcal{F}_{GL} &= \tilde{\sigma} \left(-\epsilon \Delta_S\phi + \frac{1}{\epsilon}W'(\phi) \right), \\ \mathbf{D}_\phi\mathcal{F}_H &= \frac{1}{2}\kappa'(\phi)(\mathcal{H} - \mathcal{H}_0(\phi))^2 - \kappa(\phi)(\mathcal{H} - \mathcal{H}_0(\phi))\mathcal{H}'_0(\phi). \end{aligned} \right\} \quad (\text{B7})$$

To derive the Ginzburg–Landau force $-\mathbf{D}_X\mathcal{F}_{GL}$, we use that $\delta_Y g^{ij} = -([\nabla_P Y]^{ij} + [\nabla_P Y]^{ji})$ is valid for $g_{ij} = (\partial_i X, \partial_j X)$ (Nitschke *et al.* 2022). Moreover, the relation $\delta_Y \partial_i \phi = 0$ holds, according to the assumption $\delta_Y \phi = 0$. This results in the following:

$$\begin{aligned} \delta_Y \|\nabla_S\phi\|^2 &= \delta_Y \left(g^{ij} \partial_i \phi \partial_j \phi \right) = -(\nabla_S\phi \otimes \nabla_S\phi, \nabla_P Y + (\nabla_P Y)^T) \\ &= -2(\nabla_S\phi \otimes \nabla_S\phi, \nabla_P Y), \end{aligned} \quad (\text{B8})$$

by symmetry of the outer product. With (B2) and (A9), we obtain

$$\begin{aligned} \left(\frac{\delta\mathcal{F}_{GL}}{\delta X}, \mathbf{Y} \right) &= \tilde{\sigma} \int_S -\epsilon (\nabla_S\phi \otimes \nabla_S\phi, \nabla_P Y) + \left(\frac{\epsilon}{2} \|\nabla_S\phi\|^2 + \frac{1}{\epsilon}W(\phi) \right) \text{div}_P Y \\ &= -\tilde{\sigma} \left(\epsilon \nabla_S\phi \otimes \nabla_S\phi - \left(\frac{\epsilon}{2} \|\nabla_S\phi\|^2 + \frac{1}{\epsilon}W(\phi) \right) \mathbf{P}, \nabla_P Y \right). \end{aligned} \quad (\text{B9})$$

Eventually, integration by parts (A14) yields

$$\mathbf{D}_X\mathcal{F}_{GL} = \tilde{\sigma} \text{div}_C \left(\epsilon \left(\nabla_S\phi \otimes \nabla_S\phi - \frac{\|\nabla_S\phi\|^2}{2} \mathbf{P} \right) - \frac{1}{\epsilon}W(\phi)\mathbf{P} \right) \in T\mathbb{R}^3|_S. \quad (\text{B10})$$

In terms of stress, this means that the Ginzburg–Landau energy induces a trace-free and symmetric tangential stress for phase separations and a volumetric stress for the

double-well potential. To separate the induced tangential and normal forces, we use metric compatibility $\nabla_S \mathbf{P} = 0$ and surface divergence (A13). This results in

$$\begin{aligned} \mathbf{P}D_X \mathcal{F}_{GL} &= \tilde{\sigma} \operatorname{div}_S \left(\epsilon \left(\nabla_S \phi \otimes \nabla_S \phi - \frac{\|\nabla_S \phi\|^2}{2} \mathbf{P} \right) - \frac{1}{\epsilon} W(\phi) \mathbf{P} \right) \\ &= \tilde{\sigma} \left(\epsilon \Delta_S \phi - \frac{1}{\epsilon} W'(\phi) \right) \nabla_S \phi = -(\mathbf{D}_\phi \mathcal{F}_{GL}) \nabla_S \phi \in TS, \end{aligned} \quad (\text{B11})$$

$$\begin{aligned} \mathbf{v}D_X \mathcal{F}_{GL} &= \tilde{\sigma} \left(\epsilon \left(\nabla_S \phi \otimes \nabla_S \phi - \frac{\|\nabla_S \phi\|^2}{2} \mathbf{P} \right) - \frac{1}{\epsilon} W(\phi) \mathbf{P}, \mathcal{B} \right) \\ &= \tilde{\sigma} \epsilon (\nabla_S \phi) \mathcal{B} \nabla_S \phi - \tilde{\sigma} \mathcal{H} \left(\frac{\epsilon}{2} \|\nabla_S \phi\|^2 + \frac{1}{\epsilon} W(\phi) \right) \in T^0 S. \end{aligned} \quad (\text{B12})$$

To calculate the Helfrich force $-\mathbf{D}_X \mathcal{F}_H$ we need the deformation derivative of the mean curvature. From Nitschke *et al.* (2022), we already know the tangential part of the deformation derivative of the shape operator. Explicitly, $\mathbf{P}(\partial_Y \mathcal{B})\mathbf{P} = \nabla_S(\mathbf{v} \nabla_C Y) - \mathcal{B} \nabla_P Y$, where $\partial_Y \mathcal{B}$ is to be read Cartesian-componentwise. Since tr and ∂_Y commute in this way, we obtain $\partial_Y \mathcal{H} = \operatorname{div}_S(\mathbf{v} \nabla_C Y) - (\mathcal{B}, \nabla_P Y)$. With (B2) and integration by parts for the covariant divergence, we obtain

$$\begin{aligned} \left(\frac{\delta \mathcal{F}_H}{\delta \mathbf{X}}, \mathbf{Y} \right) &= \int_S \kappa(\phi) (\mathcal{H} - \mathcal{H}_0(\phi)) \left(\partial_Y \mathcal{H} + \frac{1}{2} (\mathcal{H} - \mathcal{H}_0(\phi)) \operatorname{div}_P Y \right) \\ &= - \left(\mathbf{v} \otimes \nabla_S (\kappa(\phi) (\mathcal{H} - \mathcal{H}_0(\phi))) + \kappa(\phi) (\mathcal{H} - \mathcal{H}_0(\phi)) \right. \\ &\quad \left. \times \left(\mathcal{B} - \frac{\mathcal{H} - \mathcal{H}_0(\phi)}{2} \mathbf{P} \right), \nabla_C Y \right), \end{aligned} \quad (\text{B13})$$

and then

$$\begin{aligned} \mathbf{D}_X \mathcal{F}_H &= \operatorname{div}_C \left(\kappa(\phi) (\mathcal{H} - \mathcal{H}_0(\phi)) \left(\mathcal{B} - \frac{\mathcal{H} - \mathcal{H}_0(\phi)}{2} \mathbf{P} \right) \right. \\ &\quad \left. + \mathbf{v} \otimes \nabla_S (\kappa(\phi) (\mathcal{H} - \mathcal{H}_0(\phi))) \right), \end{aligned} \quad (\text{B14})$$

by integration by parts (A15). In terms of stress, we get an orthogonal decomposition of a trace-free and symmetric tangential stress tensor, a volumetric stress tensor scaled by $\mathcal{H}_0(\phi)$, and an additional stress tensor operating in the normal-tangential space $\mathbf{v} \otimes TS$. Using (A13), metric compatibility $\nabla_S \mathbf{P} = 0$, the fact that \mathcal{B} is curl-free and thus $\operatorname{div}_S \mathcal{B} = \nabla_S \mathcal{H}$, and $\nabla_S f(\phi) = f'(\phi) \nabla_S \phi$ for $f \in \{\kappa, \mathcal{H}_0\}$, the results in the tangential and normal Helfrich forces are

$$\begin{aligned} \mathbf{P}D_X \mathcal{F}_H &= (\kappa(\phi) (\mathcal{H} - \mathcal{H}_0(\phi)) \mathcal{H}'_0(\phi) - \frac{1}{2} \kappa'(\phi) (\mathcal{H} - \mathcal{H}_0(\phi))^2) \nabla_S \phi \\ &= -(\mathbf{D}_\phi \mathcal{F}_H) \nabla_S \phi \in TS, \end{aligned} \quad (\text{B15})$$

$$\mathbf{v}D_X\mathcal{F}_H = \Delta_S(\kappa(\phi)(\mathcal{H} - \mathcal{H}_0(\phi))) + \kappa(\phi)(\mathcal{H} - \mathcal{H}_0(\phi)) \left(\|\mathcal{B}\|^2 - \frac{\mathcal{H}}{2}(\mathcal{H} - \mathcal{H}_0(\phi)) \right). \tag{B16}$$

B.3. Dissipative forces

In this section we consider the dissipation potential $\mathcal{D} = \mathcal{D}_V + \mathcal{D}_R + \mathcal{D}_\phi$, where $\mathcal{D}_V = \int_S(\eta/4)\|\nabla_P\mathbf{u} + (\nabla_P\mathbf{u})^T\|^2$ is the viscous stress, $\mathcal{D}_R = \int_S(\gamma/2)\|\mathbf{u}\|^2$ the friction with surrounding material, and $\mathcal{D}_\phi = (1/2m)|\dot{\phi}|_{H^{-1}}^2$ the (H^{-1}) -immobility potential. Since the viscous stress potential does not depend on ϕ , we get

$$D_{\dot{\phi}}\mathcal{D}_V = 0. \tag{B17}$$

Variation with respect to \mathbf{u} gives $(\delta\mathcal{D}_V/\delta\mathbf{u}, \mathbf{Y}) = \eta(\nabla_P\mathbf{u} + (\nabla_P\mathbf{u})^T, \nabla_P\mathbf{Y})$ by symmetry. Therefore, by applying integration by parts (A14) we obtain the negative viscous force,

$$D_{\mathbf{u}}\mathcal{D}_V = -\eta \operatorname{div}_C(\nabla_P\mathbf{u} + (\nabla_P\mathbf{u})^T) \in T\mathbb{R}^3|_S, \tag{B18}$$

containing twice the tangential strain rate tensor. The friction potential does not depend on $\dot{\phi}$. Therefore, we have

$$D_{\dot{\phi}}\mathcal{D}_R = 0, \tag{B19}$$

$$D_{\mathbf{u}}\mathcal{D}_R = \gamma\mathbf{u} \in T\mathbb{R}^3|_S. \tag{B20}$$

We approach the immobility potential by defining a scalar field $\varphi[f] \in T^0\mathcal{S}$ implicitly so that it solves the equation $\Delta_S\varphi[f] = f \in T^0\mathcal{S}$. Due to this, we can write the immobility potential in a L^2 -manner by $\mathcal{D}_\phi = \frac{1}{2m} \int_S \|\nabla_S\varphi[\dot{\phi}]\|^2$. Since $\varphi[f]$ is linear in f , this yields

$$\left(\frac{\delta\mathcal{D}_\phi}{\delta\dot{\phi}}, \psi \right) = \frac{1}{m}(\nabla_S\varphi[\dot{\phi}], \nabla_S\varphi[\psi]) = -\frac{1}{m}(\varphi[\dot{\phi}], \Delta_S\varphi[\psi]) = -\frac{1}{m}(\varphi[\dot{\phi}], \psi). \tag{B21}$$

By considering $\tilde{\partial}_Y\phi = 0$, we get the dissipative forces

$$D_{\dot{\phi}}\mathcal{D}_\phi = -\frac{1}{m}\varphi[\dot{\phi}], \quad (\text{with } \Delta_S\varphi[\dot{\phi}] = \dot{\phi}), \tag{B22}$$

$$D_{\mathbf{u}}\mathcal{D}_\phi = 0. \tag{B23}$$

Note that for all sufficient smooth $f \in T^0\mathcal{S}$ and $m \neq 0$ the equation $D_{\dot{\phi}}\mathcal{D}_\phi + f = 0$ implies $\dot{\phi} = m\Delta_S f$.

B.4. Implementation of local inextensibility

The Lagrange–d’Alembert principle (B6) holds by assuming mass conservation $0 = \dot{\rho} + \rho \operatorname{div}_P\mathbf{u}$. If we also want to set $\dot{\rho} = 0$, or equivalently $\operatorname{div}_P\mathbf{u} = 0$, we have to constrain the solution space of (B6). We obtain this constraint by the Lagrange multiplier technique, where the Lagrange function $\mathcal{C}_{IE} = -\int_S p \operatorname{div}_P\mathbf{u}$ has to be included appropriately into the variation process. The Lagrange multiplier $p \in T^0\mathcal{S}$ yields a new degree of freedom,

which we associate formally to a process variable, since its purpose is to constrain the process variable \mathbf{u} . Therefore, we obtain additional negative applied forces

$$\mathbf{D}_p \mathcal{C}_{IE} = -\operatorname{div}_p \mathbf{u} \in T^0 \mathcal{S}, \tag{B24}$$

$$\mathbf{D}_u \mathcal{C}_{IE} = \operatorname{div}_C(p\mathbf{P}) = \nabla_S p + p\mathcal{H}\nu \in T\mathbb{R}^3|_{\mathcal{S}}, \tag{B25}$$

by $(\mathbf{D}_p \mathcal{C}_{IE}, q) := (\delta \mathcal{C}_{IE} / \delta p, q)$ and $(\mathbf{D}_u \mathcal{C}_{IE}, \mathbf{Y}) := (\delta \mathcal{C}_{IE} / \delta \mathbf{u}, \mathbf{Y})$, with virtual displacements $q \in T^0 \mathcal{S}$ and $\mathbf{Y} \in T\mathbb{R}^3|_{\mathcal{S}}$ and integration by parts (A16). We do not consider a variation with respect to $\dot{\phi}$, since this would result in $\mathbf{D}_{\dot{\phi}} \mathcal{C}_{IE} = 0$ anyway. Including this into (B6) gives

$$0 = (\rho \dot{\mathbf{u}} + \mathbf{D}_X \mathcal{F} + \mathbf{D}_u \mathcal{D} + \mathbf{D}_u \mathcal{C}_{IE}, \mathbf{Y}) + (\mathbf{D}_\phi \mathcal{F} + \mathbf{D}_\phi \mathcal{D}, \psi) + (\mathbf{D}_p \mathcal{C}_{IE}, q), \tag{B26}$$

for all $\mathbf{Y} \in T\mathbb{R}^3|_{\mathcal{S}}$ and $\psi, q \in T^0 \mathcal{S}$. Mutual independence of the virtual displacements leads to the strong formulation,

$$\rho \dot{\mathbf{u}} = -(\operatorname{div}_C(p\mathbf{P}) + \mathbf{D}_X \mathcal{F}_{GL} + \mathbf{D}_X \mathcal{F}_H + \mathbf{D}_u \mathcal{D}_V + \mathbf{D}_u \mathcal{D}_R), \tag{B27}$$

$$\dot{\phi} = m \Delta_S (\mathbf{D}_\phi \mathcal{F}_{GL} + \mathbf{D}_\phi \mathcal{F}_H), \tag{B28}$$

$$0 = \operatorname{div}_p \mathbf{u}, \tag{B29}$$

recalling the calculations in §§ B.2 and B.3. Since (B27) and (B29) constitute the inextensible Navier–Stokes equations with some additional forces, it is justified to call the Lagrange multiplier p , the pressure.

B.5. Total energy rate

In this section we investigate the total energy rate $(d/dt)(\mathcal{F}_K + \mathcal{F})$ comprising the sum of the kinetic energy \mathcal{F}_K and the potential energy $\mathcal{F} = \mathcal{F}_{GL} + \mathcal{F}_H$. For (B27)–(B29) to be thermodynamically consistent, it is necessary that the total energy rate only depends on the dissipation potential $\mathcal{D} = \mathcal{D}_V + \mathcal{D}_R + \mathcal{D}_\phi$, since this is the only mechanism that allows energy exchange with the surrounding of \mathcal{S} , and the total energy $\mathcal{F}_K + \mathcal{F}$ must not increase with time.

Using (B27)–(B29), including $\dot{\rho} = 0$, and applying the chain rule yields

$$\begin{aligned} \frac{d}{dt} (\mathcal{F}_K + \mathcal{F}) &= (\rho \dot{\mathbf{u}} + \mathbf{D}_X \mathcal{F}, \mathbf{u}) + (\mathbf{D}_\phi \mathcal{F}, \dot{\phi}) \\ &= -(\operatorname{div}_C(p\mathbf{P}) + \mathbf{D}_u \mathcal{D}_V + \mathbf{D}_u \mathcal{D}_R, \mathbf{u}) - \frac{1}{M} |\dot{\phi}|_{H^{-1}}^2. \end{aligned} \tag{B30}$$

Integration by parts (A16) and (A15), $\mathbf{D}_u \mathcal{D}_V$ (B18) and $\mathbf{D}_u \mathcal{D}_R$ (B20) results in

$$\left. \begin{aligned} (\operatorname{div}_C(p\mathbf{P}), \mathbf{u}) &= -(p, \operatorname{div}_p \mathbf{u}) = 0, \\ (\mathbf{D}_u \mathcal{D}_V, \mathbf{u}) &= \eta (\nabla_p \mathbf{u} + (\nabla_p \mathbf{u})^T, \nabla_p \mathbf{u}) = \frac{\eta}{2} \int_S \|\nabla_p \mathbf{u} + (\nabla_p \mathbf{u})^T\|^2, \\ (\mathbf{D}_u \mathcal{D}_R, \mathbf{u}) &= \gamma \int_S \|\mathbf{u}\|^2. \end{aligned} \right\} \tag{B31}$$

As a consequence, we finally obtain

$$\frac{d}{dt} (\mathcal{F}_K + \mathcal{F}) = -2\mathcal{D} \leq 0, \tag{B32}$$

which satisfies our requirements above.

B.6. Material time derivative

In this section we explain the material time derivative in details. Following the description in Nitschke & Voigt (2022) for scalar fields $\phi \in T^0\mathcal{S}$, the material derivative can be written as

$$\dot{\phi} = \partial_t \phi + \nabla_w \phi, \tag{B33}$$

where $w \in T^1\mathcal{S}$ is the so-called relative velocity. To be able to evaluate both summands on the right-hand side, we use the two different parametrizations $X : (t, y^1, y^2) \mapsto X(t, y^1, y^2) \in \mathcal{S}(t)$ and $X_m : (t, y_m^1, y_m^2) \mapsto X_m(t, y_m^1, y_m^2) \in \mathcal{S}(t)$. Both parametrizations describe the same moving surface, where X_m describe the material, i.e. the map $X_m|_{(y_m^1, y_m^2)} : [t_0, t_1] \rightarrow \mathbb{R}^3$ details the path of a single material particle in time. In contrast, X is arbitrary as long as it depicts the same moving surface. This means that X acts as an observer of \mathcal{S} . With this clarified, the scalar field ϕ can be represented by evaluating $\phi(t, y^1, y^2)$ as well as $\tilde{\phi}(t, \mathbf{x}(t))$, where $\mathbf{x}(t) = X(t, y^1, y^2)$ or $(y^1, y^2) = X|_t^{-1}(\mathbf{x}(t))$, respectively. To make it clear, ϕ and $\tilde{\phi}$ are the very same scalar field from a physical point of view, only the mathematical representation differs. Partial derivatives depend on the mathematical description of their argument, contrary to total derivatives, for example. Hence, we have to be careful when evaluating the first summand in (B33). This partial time derivative reads

$$\partial_t \phi(t, y^1, y^2) = \left. \frac{d}{d\tau} \right|_{\tau=0} \phi(t + \tau, y^1, y^2) = \left. \frac{d}{d\tau} \right|_{\tau=0} \tilde{\phi}(t + \tau, X(t + \tau, y^1, y^2)), \tag{B34}$$

or in terms of a differential quotient,

$$\begin{aligned} \widetilde{\partial_t \phi}(t, \mathbf{x}(t)) &= (\partial_t \phi(t, y^1, y^2))|_{(y^1, y^2) = X|_t^{-1}(\mathbf{x}(t))} \\ &= \frac{1}{\tau} (\tilde{\phi}(t + \tau, \mathbf{x}(t + \tau)) - \tilde{\phi}(t, \mathbf{x}(t))) + O(\tau), \end{aligned} \tag{B35}$$

with respect to global coordinates $\mathbf{x}(t) \in \mathcal{S}(t)$, where $\widetilde{\partial_t \phi}$ is equal to $\partial_t \phi$ due to the relation $\mathbf{x}(t) = X(t, y^1, y^2)$. As a consequence, $\partial_t \phi$ is well defined and can be discretize in time with respect to global coordinates. Since $\partial_t \phi$ represents only the observer rate of ϕ , the second summand in (B33) represents the correction to obtain the material rate. The relative velocity is given by $w = u - v$, where u is the material velocity and v the observer velocity. In local observer coordinates, they are given by

$$u(t, y^1, y^2) = \partial_t X_m(t, X_m|_t^{-1}(X(t, y^1, y^2))), \quad v(t, y^1, y^2) = \partial_t X(t, y^1, y^2). \tag{B36a,b}$$

As a consequence, we have

$$\left. \begin{aligned} \tilde{u}(t, \mathbf{x}(t)) &= u(t, y^1, y^2)|_{(y^1, y^2) = X|_t^{-1}(\mathbf{x}(t))} = (\partial_t X_m(t))|_{x_m(t) = \mathbf{x}(t)}, \\ \tilde{v}(t, \mathbf{x}(t)) &= v(t, y^1, y^2)|_{(y^1, y^2) = X|_t^{-1}(\mathbf{x}(t))} = \partial_t X(t), \end{aligned} \right\} \tag{B37}$$

where the relation between global and material local coordinates is given by $x_m(t) = X_m(t, y_m^1, y_m^2)$ or $(y_m^1, y_m^2) = X_m|_t^{-1}(x_m(t))$, respectively. Note that for geometrical reasons, $(v, v) = (u, v)$ holds. Due to this, the relative velocity is a tangential vector field, i.e. $w = u - v \in T^1\mathcal{S}$, and therefore $\nabla_w \phi = (\nabla_S \phi, w)$ is valid. Putting all together, we

can write the material derivative (B33) for $\tilde{\phi}(t, \mathbf{x}(t)) = \dot{\phi}(t, y^1, y^2)|_{(y^1, y^2)=X|_t^{-1}(\mathbf{x}(t))}$ as

$$\begin{aligned} \tilde{\phi}(t, \mathbf{x}(t)) &= \frac{1}{\tau}(\tilde{\phi}(t + \tau, \mathbf{x}(t + \tau)) - \tilde{\phi}(t, \mathbf{x}(t))) \\ &+ (\nabla_S \tilde{\phi}(t, \mathbf{x}(t)), \tilde{\mathbf{u}}(t, \mathbf{x}(t)) - \frac{1}{\tau}(\mathbf{x}(t + \tau) - \mathbf{x}(t))) + O(\tau) \end{aligned} \quad (\text{B38})$$

in terms of global coordinates and differential quotients. This representation is very suitable to implement flow equations on a surface grid that does not necessarily have to follow the material flow. Here, $\mathbf{x}(t)$ is given by the surface grid coordinates and the material velocity $\tilde{\mathbf{u}}$ is part of the solution defined on these grid coordinates. To simplify the notation in all the other sections, we do not make use of the tilde, since all the field quantities with or without the tilde are exactly the same fields. They differ only within the argument formulation, which is not used in any case outside of this section. Note that we can also apply (B33), or (B38), respectively, for the material acceleration $\dot{\mathbf{u}}$ with respect to a Cartesian frame \mathbf{e}_I . Since $\dot{\mathbf{e}}_I = 0$, the relation $\dot{\mathbf{u}} = \dot{u}^I \mathbf{e}_I$ holds, for $\mathbf{u} = u^I \mathbf{e}_I$.

There are other representations of the material derivative (B33). For instance Dziuk & Elliott (2013) stated

$$\hat{\phi}(t, \mathbf{x}_m(t)) = \partial_t \hat{\phi}(t, \mathbf{x}_m(t)) + (\nabla \hat{\phi}, \hat{\mathbf{u}}(t, \mathbf{x}_m(t))), \quad (\text{B39})$$

when rewritten in our notation (in Dziuk & Elliott (2013), the authors use a function $G(t, \cdot) : \mathcal{S}(0) \rightarrow \mathcal{S}(t)$. But we can define this map by $G(t, \mathbf{x}_m(0)) := \mathbf{x}_m(t)$ implicitly), where $\hat{\phi}(t, \mathbf{x}_m(t)) = \phi(t, y^1, y^2)$ for $(y^1, y^2) = X|_t^{-1}(\mathbf{x}_m(t))$ and $\hat{\mathbf{u}}(t, \mathbf{x}_m(t)) = \partial_t \mathbf{x}_m(t)$. As already mentioned in Dziuk & Elliott (2013), both summands on the right-hand side are not defined on a geometrically non-stationary surface, if considered individually. For the partial time derivative we have to evaluate $\hat{\phi}(t + \tau, \mathbf{x}_m(t))$ for a small time step τ . However, $\hat{\phi}|_{t+\tau}$ is only defined at future locations $\mathbf{x}_m(t + \tau) \in \mathcal{S}(t + \tau)$ and not at the current $\mathcal{S}(t)$ if no further assumptions are considered. The same applies to the second summand, which depends on the normal derivative $(\nabla \hat{\phi}, \mathbf{v})$ if the material velocity $\hat{\mathbf{u}}$ comprises a normal velocity. Such a normal derivative cannot be obtained without considering its extensions outside of the surface. One might be tempted to interpret (B39) as a fully Eulerian perspective, since $(\partial_t \hat{\phi})|_{\mathbf{x}_m(t)=X(t, y^1, y^2)} = \partial_t \phi$ is valid for $\partial_t X = 0$. However, a fully Eulerian surface observer does not exist if the surface comprises a flow in the normal direction. Any normal part of the surface motion has to be treated in a Lagrangian perspective at least. In general, (B39) is equal to (B33), since $(\partial_t \hat{\phi})|_{\mathbf{x}_m(t)=X(t, y^1, y^2)} = \partial_t \phi - (\nabla \phi, \mathbf{v})$ holds formally in arbitrary observer coordinates.

Appendix C. Non-dimensionalization

In order to non-dimensionalize the model in Problem 2.1, we write the rescaled variables by using the symbol $\hat{\cdot}$. We define the rescaled parametrization $X = \hat{X}L$, the velocity $\mathbf{u} = \hat{\mathbf{u}}U$, the mean curvature $\mathcal{H} = \hat{\mathcal{H}}/L$, the phase field $\phi = \hat{\phi}$ and the chemical potential $\mu = \rho \hat{\mu}U^2$ for the characteristic length L and a characteristic velocity U , which defines a rescaled time $t = L/U\hat{t}$. According to the parametrization, we rescale the gradient of the embedded space by $\nabla = \hat{\nabla}/L$. This rescales the surface operators accordingly, for example, the material time derivative reads $(\partial_t + \nabla_w) = U/L(\partial_{\hat{t}} + \hat{\nabla}_{\hat{w}})$. We introduce

the rescaled material functions, $\hat{\kappa}(\phi) = \kappa(\phi)/(\rho U^2 L^2)$, $\hat{\mathcal{H}}_0(\phi) = \mathcal{H}_0(\phi)L$, and $\hat{W}(\phi) = 1/L^2 W(\phi)$; and the rescaled material parameters $Re = \rho LU/\eta$, denoting the Reynolds number, $\hat{m} = \rho m U/L$, $\hat{\sigma} = \tilde{\sigma}/(\rho U^2 L^2)$, and $\hat{\gamma} = \gamma L/(\rho U)$. Considering the rescaled variables and replacing the material functions and parameters into the model, we obtain the following non-dimensional system:

$$\left. \begin{aligned} \partial_t \hat{\phi} + \hat{\nabla}_w \hat{\phi} &= \hat{m} \hat{\Delta}_S \hat{\mu}, \\ \hat{\mu} &= -\hat{\sigma} \epsilon \hat{\Delta}_S \hat{\phi} + \frac{\tilde{\sigma}}{\epsilon} \hat{W}'(\hat{\phi}) + \frac{\hat{\kappa}'}{2}(\hat{\phi}) (\hat{\mathcal{H}} - \hat{\mathcal{H}}_0(\hat{\phi}))^2 - \hat{\kappa}(\hat{\phi}) \hat{\mathcal{H}}'_0(\hat{\phi}) (\hat{\mathcal{H}} - \hat{\mathcal{H}}_0(\hat{\phi})), \\ \partial_t \hat{\mathbf{u}} + \hat{\nabla}_w \hat{\mathbf{u}} &= -\hat{\nabla}_{SP} - p \hat{\mathcal{H}} \mathbf{v} + \frac{2}{Re} \text{div}_C \hat{\boldsymbol{\sigma}} - \hat{\gamma} \hat{\mathbf{u}} + \hat{\mathbf{b}}_T + \hat{\mathbf{b}}_N, \\ \text{div}_p \hat{\mathbf{u}} &= 0, \end{aligned} \right\} \tag{C1}$$

where $\hat{\mathbf{b}}_T$ and $\hat{\mathbf{b}}_N$ correspond to the rescaled tangential and normal bending terms, respectively. In the main sections of the paper, we drop the symbol $\hat{\cdot}$ for better readability.

Material parameters for surface viscosity and bending rigidity of biomembranes made of typical lipids are reported in Faizi *et al.* (2022). They range from 10^0 – 10^6 nPa s m for the surface viscosity and 10^1 – 10^2 k_BT for the bending rigidity. The value for the surface viscosity and surface density corresponds to $\eta = \eta_{3D} \xi$ and $\rho = \rho_{3D} \xi$ where ξ is the surface thickness and η_{3D} and ρ_{3D} are the material viscosity and density, respectively. Using appropriate values for L , U and ξ these quantities can be related to the considered parameter range.

Appendix D. Derivation of the overdamped limit model

We consider the overdamped limit of the model in Problem 2.2. We define the rescaled parameters $\delta = 1/\gamma$, $\tilde{\sigma} = \delta \tilde{\sigma}$, $\tilde{\kappa} = \delta \kappa$ and $\tilde{m} = m/\delta$, and the rescaled variables $\tilde{p} = \delta p$ and $\tilde{\mu} = \delta \mu$. Substituting these parameters and variables into the model, we get

$$\left. \begin{aligned} \partial_t \phi + \nabla_w \phi &= \tilde{m} \Delta_S \tilde{\mu}, \\ \tilde{\mu} &= \tilde{\sigma} \left(-\epsilon \Delta_S \phi + \frac{1}{\epsilon} W'(\phi) \right) + \frac{1}{2} \tilde{\kappa}'(\phi) (\mathcal{H} - \mathcal{H}_0(\phi))^2 \\ &\quad - \tilde{\kappa}(\phi) \mathcal{H}'_0(\phi) (\mathcal{H} - \mathcal{H}_0(\phi)), \\ \delta \partial_t \mathbf{u} + \delta \nabla_w \mathbf{u} &= -\nabla_S \tilde{p} - \tilde{p} \mathcal{H} \mathbf{v} + \frac{2\delta}{Re} \text{div}_p \boldsymbol{\sigma} - \mathbf{u} + \tilde{\mathbf{b}}_T + \tilde{\mathbf{b}}_N, \\ \text{div}_p \mathbf{u} &= 0, \end{aligned} \right\} \tag{D1}$$

where $\tilde{\mathbf{b}}_T$ and $\tilde{\mathbf{b}}_N$ are the tangential and normal forces with respect to the rescaled variables and $\mathbf{w} = \mathbf{u} - \partial_t \mathbf{X}$ as before. The overdamped limit is then obtained by considering $\delta \searrow 0$, and it reads

$$\partial_t \phi + \nabla_w \phi = \tilde{m} \Delta_S \tilde{\mu}, \tag{D2}$$

$$\begin{aligned} \tilde{\mu} &= \tilde{\sigma} \left(-\epsilon \Delta_S \phi + \frac{1}{\epsilon} W'(\phi) \right) + \frac{1}{2} \tilde{\kappa}'(\phi) (\mathcal{H} - \mathcal{H}_0(\phi))^2 \\ &\quad - \tilde{\kappa}(\phi) \mathcal{H}'_0(\phi) (\mathcal{H} - \mathcal{H}_0(\phi)), \end{aligned} \tag{D3}$$

$$\mathbf{u} = -\nabla_S \tilde{p} - \tilde{p} \mathcal{H} \mathbf{v} + \tilde{\mathbf{b}}_T + \tilde{\mathbf{b}}_N, \quad (\text{D4})$$

$$\text{div}_P \mathbf{u} = 0. \quad (\text{D5})$$

Considering $\mathbf{u}_T = P\mathbf{u}$ and $u_N = \mathbf{u} \cdot \mathbf{v}$, (D4) can be split into a tangential and a normal part. Substituting these terms in (D5) and using the definitions for $\tilde{\mathbf{b}}_T$ and $\tilde{\mathbf{b}}_N$ we obtain

$$\left. \begin{aligned} \partial_t \phi + \nabla_w \phi &= \tilde{m} \Delta_S \tilde{\mu}, \\ \tilde{\mu} &= \tilde{\sigma} \left(-\epsilon \Delta_S \phi + \frac{1}{\epsilon} W'(\phi) \right) + \frac{1}{2} \tilde{\kappa}'(\phi) (\mathcal{H} - \mathcal{H}_0(\phi))^2 \\ &\quad - \tilde{\kappa}(\phi) \mathcal{H}'_0(\phi) (\mathcal{H} - \mathcal{H}_0(\phi)), \\ u_N &= -\tilde{p} \mathcal{H} + \tilde{\mathbf{b}}_N, \\ \mathbf{u}_T &= -\nabla_S \tilde{p} + \tilde{\mu} \nabla_S \phi, \\ -\Delta_S \tilde{p} + \tilde{p} \mathcal{H}^2 &= -\text{div}_S(\tilde{\mu} \nabla_S \phi) + \tilde{\mathbf{b}}_N \mathcal{H}, \end{aligned} \right\} \quad (\text{D6})$$

where $\tilde{\mathbf{b}}_N$ is given by

$$\begin{aligned} \tilde{\mathbf{b}}_N &= \tilde{\mathbf{b}}_N \cdot \mathbf{v} \\ &= -\Delta_S(\kappa(\phi)(\mathcal{H} - \mathcal{H}_0(\phi))) - \kappa(\phi)(\mathcal{H} - \mathcal{H}_0(\phi))(\|\mathcal{B}\|^2 - \frac{1}{2}\mathcal{H}(\mathcal{H} - \mathcal{H}_0(\phi))) \\ &\quad + \tilde{\sigma} \left(\frac{\epsilon}{2} \|\nabla_S \phi\|^2 + \frac{1}{\epsilon} W(\phi) \right) \mathcal{H} - \tilde{\sigma} \epsilon \nabla_S \phi^T \mathcal{B} \nabla_S \phi. \end{aligned} \quad (\text{D7})$$

This model is closely related to a model discussed in Haußer *et al.* (2013). To perform the comparison, we recall that the total time derivative of the potential energy considered in § B.5 is given by

$$\frac{d}{dt} \mathcal{F} = (\dot{\phi}, \mathbf{D}_\phi \mathcal{F}) + (\mathbf{u}, \mathbf{D}_X \mathcal{F}). \quad (\text{D8})$$

In Haußer *et al.* (2013), the material derivative $\dot{\phi}$ is reduced to the partial time derivative $\partial_t \phi$, and this leads to the differences noted between the models.

More commonly used models reduce the local inextensibility constraint and only consider a global area constraint

$$\int_S \text{div}_P \mathbf{u} dS = \int_S \text{div}_S \mathbf{u}_T - u_N \mathcal{H} dS = - \int_S u_N \mathcal{H} dS = 0, \quad (\text{D9})$$

which can be realized by

$$\tilde{p} = \frac{\int_S u_N \mathcal{H} dS}{\int_S \mathcal{H} dS}. \quad (\text{D10})$$

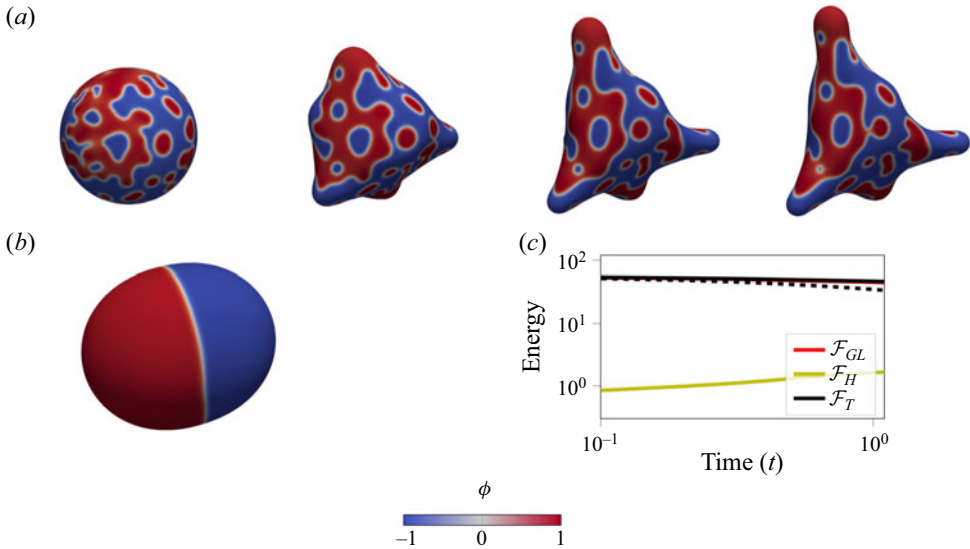


Figure 6. (a) Snapshots of the relaxation of the two-component elastic surface (without hydrodynamics) (D12), with random initial condition ϕ_1 for $t = 0, 0.3, 0.8, 1.1$, with constant bending stiffness $\kappa_1 = \kappa_2 = \kappa = 0.02$ and $\mathcal{H}_0 = 0$. The phase field ϕ is visualized. The time instances correspond to the simulation of the full model shown in figure 2(a). (b) Reached equilibrium configuration for the same configuration as in (a) but with $\kappa = 0.5$. (c) Energy over time for the Ginsburg–Landau energy \mathcal{F}_{GL} , the Helfrich energy \mathcal{F}_H and total energy \mathcal{F}_T , corresponding to (a). The black dashed line shows the total energy of the simulation in figure 2(a) for comparison.

In this case \tilde{p} and \mathbf{u}_T are independent. The corresponding system reads

$$\left. \begin{aligned}
 \partial_t \phi + \nabla_{\mathbf{w}} \phi &= \tilde{m} \Delta_S \tilde{\mu}, \\
 \tilde{\mu} &= \tilde{\sigma} \left(-\epsilon \Delta_S \phi + \frac{1}{\epsilon} W'(\phi) \right) + \frac{1}{2} \tilde{\kappa}'(\phi) (\mathcal{H} - \mathcal{H}_0(\phi))^2 \\
 &\quad - \tilde{\kappa}(\phi) \mathcal{H}'_0(\phi) (\mathcal{H} - \mathcal{H}_0(\phi)), \\
 \mathbf{u}_N &= -\tilde{p} \mathcal{H} + \tilde{\mathbf{b}}_N, \\
 \mathbf{u}_T &= \tilde{\mu} \nabla_S \phi, \\
 \tilde{p} &= \frac{\int_S \tilde{\mathbf{b}}_N \mathcal{H} \, dS}{\int_S \mathcal{H} \, dS},
 \end{aligned} \right\} \quad (\text{D11})$$

with $\mathbf{w} = \mathbf{u}_T + u_N \mathbf{v} - \partial_t \mathbf{X}$. This system has also been considered in Haußer *et al.* (2013) and shows the same conceptual differences discussed above.

All these derivations contain the tangential velocity component $\tilde{\mu} \nabla_S \phi$. In other previous non-hydrodynamic models this term is not present Elliott & Stinner (2010a) as only variations in normal direction are considered. The model in Elliott & Stinner (2010a) but with phase-dependent spontaneous curvature $\mathcal{H}_0(\phi)$, phase-dependent bending rigidity $\tilde{\kappa}(\phi)$ and local inextensibility constraint instead of a penalization approach to

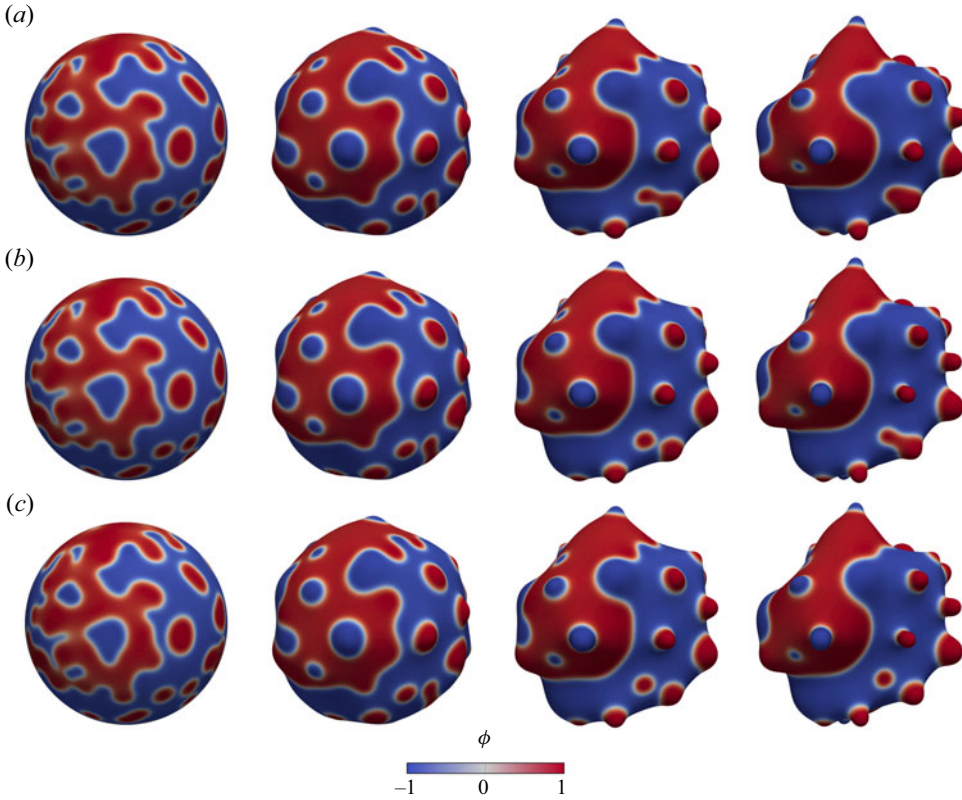


Figure 7. Snapshots of the relaxation of the two-component fluid deformable surface with random initial condition ϕ_1 and $Re = 1.0$ for $t = 0, 0.3, 0.8, 1.1$ (from left to right), with constant bending stiffness $\kappa_1 = \kappa_2 = \kappa = 0.02$ and $\mathcal{H}_0 = \gamma = 0$. (a) Semi-implicit Euler scheme (identical with figure 2a). (b,c) Corresponding results for the fully implicit iterative Euler scheme for two different time steps τ . (a) Semi-implicit Euler scheme $\tau = 0.005$, (b) iterative Euler scheme $\tau = 0.005$ and (c) iterative Euler scheme $\tau = 0.02$.

enforce the global area constraint reads

$$\left. \begin{aligned}
 \partial_t \phi + \nabla_w \phi &= \tilde{m} \Delta_S \tilde{\mu}, \\
 \tilde{\mu} &= \tilde{\sigma} \left(-\epsilon \Delta_S \phi + \frac{1}{\epsilon} W'(\phi) \right) + \frac{1}{2} \tilde{\kappa}'(\phi) (\mathcal{H} - \mathcal{H}_0(\phi))^2 \\
 &\quad - \tilde{\kappa}(\phi) \mathcal{H}'_0(\phi) (\mathcal{H} - \mathcal{H}_0(\phi)), \\
 u_N &= -\tilde{p} \mathcal{H} + \tilde{b}_N, \\
 \mathbf{u}_T &= -\nabla_S p, \\
 -\Delta_S \tilde{p} + \tilde{p} \mathcal{H}^2 &= \tilde{b}_N \mathcal{H},
 \end{aligned} \right\} \quad (D12)$$

with $\mathbf{w} = \mathbf{u}_T + u_N \mathbf{v} - \partial_t \mathbf{X}$ and \tilde{b}_N as above. This system is solved numerically using the same parameter setting as considered for figure 2(a). The results are shown in figure 6. The missing tangential transport of the interface leads to qualitative different results. The evolution strongly depends on the initial configuration and mostly deforms large patches. The characteristic bulges in figure 2(a) formed to locally reduce the interface length are not present. Also, the evolution is slower as demonstrated by the plots of the energies

in [figure 6](#). The same setting but with $\kappa = 0.5$ converges to a similar configuration as the corresponding equilibrium configurations shown in [figure 5](#).

Appendix E. Numerical justification of the considered discretization approach

To further justify the considered numerical discretization we compare the results from [figure 2\(a\)](#) with a fully implicit iterative Euler scheme. In this scheme, we iterate Problems 3.1 and 3.2 within each time step until convergence and update all unknowns in each iteration. We indicate convergence by $\|\mathcal{S}^i - \mathcal{S}^{i-1}\| + \|\mathbf{u}^i - \mathbf{u}^{i-1}\| + \|\phi^i - \phi^{i-1}\| < \delta$ for $\delta = 10^{-4}$ and \cdot^i the quantities at iteration i . [Figure 7](#) shows the phase field variable ϕ and the shape as in [figure 2\(a\)](#) together with the corresponding time instances for the fully implicit iterative Euler scheme for different time steps.

By using the same time step (comparing [figure 2a](#) with [figure 2b](#)) we obtain visually almost identical results. A more quantitative comparison provides the first pinch-off at time $t = 1.1$ for the scheme considered in the paper and at $t = 0.9$ for the iterative Euler scheme. On average the iterative Euler scheme requires four iterations to reach convergence. This reduction by a factor of four, with the same time step, makes the detailed investigations in this paper feasible. The fully implicit iterative Euler scheme can be assumed to be unconditionally energy stable. Increasing the time step by a factor of four indeed leads to qualitatively similar results, see [figure 7\(c\)](#), but also to more iterations to reach convergence (approximately seven). Further increasing the time step further increases the number of iterations or even leads to qualitatively different results. The considered scheme and time step thus not only turns out to be the most efficient it also respects an upper bound on the time step to achieve the desired accuracy. With additional results on the numerical analysis of such highly coupled surface equations further improvement on the numerical scheme is certainly possible.

REFERENCES

- ABELS, H. 2009 On a diffuse interface model for two-phase flows of viscous, incompressible fluids with matched densities. *Arch. Rat. Mech. Anal.* **194**, 463–506.
- ABELS, H., GARCKE, H. & GRÜN, G. 2012 Thermodynamically consistent, frame indifferent diffuse interface models for incompressible two-phase flows with different densities. *Math. Models Meth. Appl. Sci.* **22**, 1150013.
- AL-IZZI, S.C., SENS, P. & TURNER, M.S. 2020 Shear-driven instabilities of membrane tubes and dynamin-induced scission. *Phys. Rev. Lett.* **125**, 018101.
- ALAND, S. & VOIGT, A. 2012 Benchmark computations of diffuse interface models for two-dimensional bubble dynamics. *Intl J. Numer. Meth. Fluids* **69**, 747–761.
- ALKÄMPER, M., DEDNER, A., KLÖFKORN, R. & NOLTE, M. 2014 The dune-alugrid module. [arXiv:1407.6954](https://arxiv.org/abs/1407.6954).
- AMBRUS, V.E., BUSUIOC, S., WAGNER, A.J., PAILLUSSON, F. & KUSUMAATMAJA, H. 2019 Multicomponent flow on curved surfaces: a vielbein lattice Boltzmann approach. *Phys. Rev. E* **100**, 063306.
- ARROYO, M. & DESIMONE, A. 2009 Relaxation dynamics of fluid membranes. *Phys. Rev. E* **79**, 031915.
- BACHINI, E., BRANDNER, P., JANKUHN, T., NESTLER, M., PRAETORIUS, S., REUSKEN, A. & VOIGT, A. 2023a Diffusion of tangential tensor fields: numerical issues and influence of geometric properties. *J. Numer. Math.* <https://doi.org/10.1515/jnma-2022-0088>.
- BACHINI, E., KRAUSE, V. & VOIGT, A. 2023b The interplay of geometry and coarsening in multicomponent lipid vesicles under the influence of hydrodynamics. *Phys. Fluids* **35**, 042102.
- BARRETT, J.W., GARCKE, H. & NÜRNBERG, R. 2008 On the parametric finite element approximation of evolving hypersurfaces in \mathbb{R}^3 . *J. Comput. Phys.* **227**, 4281–4307.
- BARRETT, J.W., GARCKE, H. & NÜRNBERG, R. 2015 Numerical computations of the dynamics of fluidic membranes and vesicles. *Phys. Rev. E* **92**, 052704.
- BAUMGART, T., DAS, S., WEBB, W.W. & JENKINS, J.T. 2005 Membrane elasticity in giant vesicles with lipid phase coexistence. *Biophys. J.* **89**, 1067–1080.

- BAUMGART, T., HESS, S.T. & WEBB, W.W. 2003 Imaging coexisting fluid domains in biomembrane models coupling curvature and line tension. *Nature* **425**, 821–824.
- BENES, M., KOLAR, M., SISCHKA, J.M. & VOIGT, A. 2023 Degenerate area preserving surface Allen-Cahn equation and its sharp interface limit. [arXiv:2303.04018](https://arxiv.org/abs/2303.04018).
- BONITO, A., DEMLOW, A. & LICHT, M. 2020 A divergence-conforming finite element method for the surface Stokes equation. *SIAM J. Numer. Anal.* **58**, 2764–2798.
- BRANDNER, P., JANKUHN, T., PRAETORIUS, S., REUSKEN, A. & VOIGT, A. 2022a Finite element discretization methods for velocity-pressure and stream function formulations of surface Stokes equations. *SIAM J. Sci. Comput.* **44**, A1807–A1832.
- BRANDNER, P. & REUSKEN, A. 2020 Finite element error analysis of surface Stokes equations in stream function formulation. *ESAIM Math. Modelling Numer. Anal.* **54**, 2069–2097.
- BRANDNER, P., REUSKEN, A. & SCHWERING, P. 2022b On derivations of evolving surface Navier–Stokes equations. *Interfaces Free Bound.* **24**, 533–563.
- CAMLAY, B.A. & BROWN, F.L.H. 2011 Dynamic scaling in phase separation kinetics for quasi-two-dimensional membranes. *J. Chem. Phys.* **135**, 225106.
- DEMLOW, A. 2009 Higher-order finite element methods and pointwise error estimates for elliptic problems on surfaces. *SIAM J. Numer. Anal.* **47**, 805–827.
- DEMONT, T.H.B., VAN ZWIETEN, G.J., DIDDENS, C. & VAN BRUMMELEN, E.H. 2022 A robust and accurate adaptive approximation method for a diffuse-interface model of binary-fluid flows. *Comput. Meth. Appl. Mech. Engng* **400**, 115563.
- DESERNO, M. 2015 Fluid lipid membranes: from differential geometry to curvature stresses. *Chem. Phys. Lipids* **185**, 11–45.
- DZIUK, G. 2008 Computational parametric Willmore flow. *Numer. Math.* **111**, 55–80.
- DZIUK, G. & ELLIOTT, C.M. 2013 Finite element methods for surfaces PDEs. *Acta Numerica* **22**, 289–396.
- ELLIOTT, C.M., HATCHER, L. & STINNER, B. 2022 On the sharp interface limit of a phase field model for near spherical two phase biomembranes. *Interfaces Free Bound.* **24**, 263–286.
- ELLIOTT, C.M. & STINNER, B. 2010a Modeling and computation of two phase geometric biomembranes using surface finite elements. *J. Comput. Phys.* **229**, 6585–6612.
- ELLIOTT, C.M. & STINNER, B. 2010b A surface phase field model for two-phase biological membranes. *SIAM J. Appl. Maths* **70**, 2904–2928.
- ELSON, E.L., FRIED, E., DOLBOW, J.E. & GENIN, G.M. 2010 Phase separation in biological membranes: integration of theory and experiment. *Annu. Rev. Biophys.* **39**, 207–266.
- FAIZI, H.A., DIMOVA, R. & VLAHOVSKA, P.M. 2022 A vesicle microrheometer for high-throughput viscosity measurements of lipid and polymer membranes. *Biophys. J.* **121**, 910–918.
- FAN, J., HAN, T. & HAATAJA, M. 2010 Hydrodynamic effects on spinodal decomposition kinetics in planar lipid bilayer membranes. *J. Chem. Phys.* **133**, 235101.
- FONDA, P., RINALDIN, M., KRAFT, D.J. & GIOMI, L. 2018 Interface geometry of binary mixtures on curved substrates. *Phys. Rev. E* **98**, 032801.
- FONDA, P., RINALDIN, M., KRAFT, D.J. & GIOMI, L. 2019 Thermodynamic equilibrium of binary mixtures on curved surfaces. *Phys. Rev. E* **100**, 032604.
- FRIES, T. 2018 Higher-order surface FEM for incompressible Navier–Stokes flows on manifolds. *Intl J. Numer. Meth. Fluids* **88**, 55–78.
- GARCKE, H., KAMPMANN, J., RÄTZ, A. & RÖGER, M. 2016 A coupled surface Cahn-Hilliard bulk-diffusion system modeling lipid raft formation in cell membranes. *Math. Models Meth. Appl. Sci.* **26**, 1149–1189.
- GERA, P. & SALAC, D. 2018 Modeling of multicomponent three-dimensional vesicles. *Comput. Fluids* **172**, 362–383.
- HAIRER, E., HOCHBRUCK, M., ISERLES, A. & LUBICH, C. 2006 Geometric numerical integration. *Oberwolfach Rep.* **3**, 805–882.
- HANSBO, P., LARSON, M. & LARSSON, K. 2020 Analysis of finite element methods for vector Laplacians on surfaces. *IMA J. Numer. Anal.* **40**, 1652–1701.
- HARDERING, H. & PRAETORIUS, S. 2022 Tangential errors of tensor surface finite elements. *IMA J. Numer. Anal.* **43** (3), 1543–1585.
- HAUSSER, F., MARTH, W., LI, S., LOWENGRUB, J., RÄTZ, A. & VOIGT, A. 2013 Thermodynamically consistent models for two-component vesicles. *Intl J. Biomath. Biostat.* **2**, 19–48.
- HENLE, M.L. & LEVINE, A.J. 2010 Hydrodynamics in curved membranes: the effect of geometry on particulate mobility. *Phys. Rev. E* **81**, 011905.
- IZADI, M. & SANYAL, A. 2014 Rigid body attitude estimation based on the Lagrange–D’Alembert principle. *Automatica* **50**, 2570–2577.
- JANKUHN, T., OLSHANSKII, M.A. & REUSKEN, A. 2018 Incompressible fluid problems on embedded surfaces: modeling and variational formulations. *Interfaces Free Bound.* **20**, 353–377.

- JANKUHN, T. & REUSKEN, A. 2020 Trace finite element methods for surface vector-Laplace equations. *IMA J. Numer. Anal.* **41**, 48–83.
- JIANG, Y., LOOKMAN, T. & SAXENA, A. 2000 Phase separation and shape deformation of two-phase membranes. *Phys. Rev. E* **61**, R57.
- JÜLICHER, F. & LIPOWSKY, R. 1996 Shape transformations of vesicles with intramembrane domains. *Phys. Rev. E* **53**, 2670–2693.
- KAKSONEN, M. & ROUX, A. 2018 Mechanisms of clathrin-mediated endocytosis. *Nat. Rev. Mod. Cell Bio.* **19**, 313–326.
- KHANWALE, M.A., LOFQUIST, A.D., SUNDAR, H., ROSSMANITH, J.A. & GANAPATHYSUBRAMANIAN, B. 2020 Simulating two-phase flows with thermodynamically consistent energy stable Cahn-Hilliard-Navier-Stokes equations on parallel adaptive octree based meshes. *J. Comput. Phys.* **419**, 109674.
- KHANWALE, M.A., SAURABH, K., ISHII, M., SUNDAR, H., ROSSMANITH, J.A. & GANAPATHY-SUBRAMANIAN, B. 2023 A projection-based, semi-implicit time-stepping approach for the Cahn-Hilliard-Navier-Stokes equations on adaptive octree meshes. *J. Comput. Phys.* **475**, 111874.
- KRAUSE, V. & VOIGT, A. 2023 A numerical approach for fluid deformable surfaces with conserved enclosed volume. *J. Comput. Phys.* **486**, 112097.
- KUMAR, P.B.S., GOMPPER, G. & LIPOWSKY, R. 2001 Budding dynamics of multicomponent membranes. *Phys. Rev. Lett.* **86**, 3911.
- LEDERER, P., LEHRENFELD, C. & SCHOEBERL, J. 2020 Divergence-free tangential finite element methods for incompressible flows on surfaces. *Intl J. Numer. Meth. Engng* **121**, 2503–2533.
- LIPOWSKY, R. & DIMOVA, R. 2021 Introduction to remodeling of biomembranes. *Soft Matt.* **17**, 214–221.
- LOWENGRUB, J.S., RÄTZ, A. & VOIGT, A. 2009 Phase-field modeling of the dynamics of multicomponent vesicles: spinodal decomposition, coarsening, budding, and fission. *Phys. Rev. E* **79**, 031926.
- LOWENGRUB, J.S. & TRUSKINOVSKY, L. 1998 Quasi-incompressible Cahn-Hilliard fluids and topological transitions. *Proc. R. Soc. Lond. A* **454**, 2617–2654.
- MAGALETTI, F., PICANO, F., CHINAPPI, M., MARINO, L. & CASCIOLA, C.M. 2013 The sharp-interface limit of the Cahn-Hilliard/Navier-Stokes model for binary fluids. *J. Fluid Mech.* **714**, 95–126.
- MARSDEN, J.E. & RATIU, T.S. 2013 *Introduction to Mechanics and Symmetry: A Basic Exposition of Classical Mechanical Systems*, vol. 17. Springer Science & Business Media.
- MARSDEN, J.E. & WEST, M. 2001 Discrete mechanics and variational integrators. *Acta Numerica* **10**, 357–514.
- MCMAHON, H.T. & GALLOP, J.L. 2005 Membrane curvature and mechanisms of dynamic cell membrane remodelling. *Nature* **438**, 590–596.
- MIETKE, A., JEMSEENA, V., KUMAR, K.V., SBALZARINI, I.F. & JÜLICHER, F. 2019 Minimal model of cellular symmetry breaking. *Phys. Rev. Lett.* **123**, 188101.
- NESTLER, M., NITSCHKE, I., PRAETORIUS, S. & VOIGT, A. 2018 Orientational order on surfaces: the coupling of topology, geometry, and dynamics. *J. Nonlinear Sci.* **28**, 147–191.
- NESTLER, M., NITSCHKE, I. & VOIGT, A. 2019 A finite element approach for vector- and tensor-valued surface PDEs. *J. Comput. Phys.* **389**, 48–61.
- NESTLER, M. & VOIGT, A. 2023a A diffuse interface approach for vector-valued PDES on surfaces. [arXiv:2303.07135](https://arxiv.org/abs/2303.07135).
- NESTLER, M. & VOIGT, A. 2023b Stability of rotating equilibrium states of fluid deformable surfaces. *Proc. Appl. Math. Mech.* **2023**, e202300044.
- NITSCHKE, I., REUTHER, S. & VOIGT, A. 2017 Discrete exterior calculus (DEC) for the surface Navier-Stokes equation. In *Transport Processes at Fluidic Interfaces* (ed. D. Bothe & A. Reusken), pp. 177–197. Springer International Publishing.
- NITSCHKE, I., SADIK, S. & VOIGT, A. 2022 Tangential tensor fields on deformable surfaces – How to derive consistent L^2 -gradient flows. [arXiv:2209.13272](https://arxiv.org/abs/2209.13272).
- NITSCHKE, I. & VOIGT, A. 2022 Observer-invariant time derivatives on moving surfaces. *J. Geom. Phys.* **173**, 104428.
- NITSCHKE, I., VOIGT, A. & WENSCH, J. 2012 A finite element approach to incompressible two-phase flow on manifolds. *J. Fluid Mech.* **708**, 418–438.
- OLSHANSKII, M. 2023 On equilibrium states of fluid membranes. *Phys. Fluids* **35** (6), 062111.
- OLSHANSKII, M., PALZHANOV, Y. & QUAINI, A. 2022 A comparison of Cahn-Hilliard and Navier-Stokes-Cahn-Hilliard models on manifolds. *Vietnam J. Math.* **50**, 929–945.
- OLSHANSKII, M. & YUSHUTIN, V. 2019 A penalty finite element method for a fluid system posed on embedded surface. *J. Math. Fluid Mech.* **21**, 14–31.
- OLSHANSKII, M.A., QUAINI, A., REUSKEN, A. & YUSHUTIN, V. 2018 A finite element method for the surface Stokes problem. *SIAM J. Sci. Comput.* **40**, A2492–A2518.

- PRAETORIUS, S. & STENGER, F. 2020 DUNE-CurvedGrid—A DUNE module for surface parametrization. *Arch. Num. Software* **22**, 1–22.
- REUSKEN, A. 2018 Stream function formulation of surface Stokes equations. *IMA J. Numer. Anal.* **40**, 109–139.
- REUTHER, S., NITSCHKE, I. & VOIGT, A. 2020 A numerical approach for fluid deformable surfaces. *J. Fluid Mech.* **900**, R8.
- REUTHER, S. & VOIGT, A. 2015 The interplay of curvature and vortices in flow on curved surfaces. *Multiscale Model. Sim.* **13**, 632–643.
- REUTHER, S. & VOIGT, A. 2016 Incompressible two-phase flows with an inextensible Newtonian fluid interface. *J. Comput. Phys.* **322**, 850–858.
- REUTHER, S. & VOIGT, A. 2018a Erratum: “The interplay of curvature and vortices in flow on curved surfaces”. *Multiscale Model. Sim.* **16**, 1448–1453.
- REUTHER, S. & VOIGT, A. 2018b Solving the incompressible surface Navier–Stokes equation by surface finite elements. *Phys. Fluids* **30**, 012107.
- RINALDIN, M., FONDA, P., GIOMI, L. & KRAFT, D.J. 2020 Geometric pinning and antimixing in scaffolded lipid vesicles. *Nat. Commun.* **11**, 4314.
- SAFFMAN, P.G. & DELBRÜCK, M. 1975 Brownian motion in biological membranes. *Proc. Natl Acad. Sci. USA* **72**, 3111–3113.
- SANDER, O. 2020 *DUNE – The Distributed and Unified Numerics Environment*. Springer.
- SHEN, J. & YANG, X. 2010a Decoupled, energy stable schemes for phase-field models of two-phase incompressible flows. *SIAM J. Numer. Anal.* **53**, 279–296.
- SHEN, J. & YANG, X. 2010b Numerical approximations of Allen–Cahn and Cahn–Hilliard equations. *Discrete Contin. Dyn. Syst.* **28**, 1669–1691.
- SOHN, J.S., TSENG, J.S., LI, S., VOIGT, A. & LOWENGRUB, J.S. 2010 Dynamics of multicomponent vesicles in a viscous fluid. *J. Comput. Phys.* **229**, 119–144.
- TEN EIKELDER, M.F.P., VAN DER ZEE, K.G., ARKERMANN, I. & SCHILLINGER, D. 2023 A unified framework for Navier–Stokes–Cahn–Hilliard models with non-matching densities. *Math. Model. Meth. Appl. Sci.* **33**, 175–221.
- TORRES-SÁNCHEZ, A., MILLÁN, D. & ARROYO, M. 2019 Modelling fluid deformable surfaces with an emphasis on biological interfaces. *J. Fluid Mech.* **872**, 218–271.
- UDWADIA, F.E. & KALABA, R.E. 2002 On the foundations of analytical dynamics. *Intl J. Non-Linear Mech.* **37**, 1079–1090.
- VEATCH, S.L. & KELLER, S.L. 2003 Separation of liquid phases in giant vesicles of ternary mixtures of phospholipids and cholesterol. *Biophys. J.* **85**, 3074–3083.
- VEATCH, S.L., SOUBIAS, O., KELLER, S.L. & GAWRISCH, K. 2007 Critical fluctuations in domain-forming lipid mixtures. *Proc. Natl Acad. Sci. USA* **104**, 17650–17655.
- VEY, S. & VOIGT, A. 2007 AMDiS: adaptive multidimensional simulations. *Comput. Vis. Sci.* **10**, 57–67.
- WANG, X. & DU, Q. 2008 Modelling and simulations of multi-component lipid membranes and open membranes via diffuse interface approaches. *J. Math. Biol.* **56**, 347–371.
- WITKOWSKI, T., LING, S., PRAETORIUS, S. & VOIGT, A. 2015 Software concepts and numerical algorithms for a scalable adaptive parallel finite element method. *Adv. Comput. Math.* **41**, 1145–1177.
- WOODHOUSE, F.G. & GOLDSTEIN, R.E. 2012 Shear-driven circulation patterns in lipid membrane vesicles. *J. Fluid Mech.* **705**, 165–175.
- ZHANG, T. & WOLGEMUTH, C.W. 2022 A general computational framework for the dynamics of single- and multi-phase vesicles and membranes. *J. Comput. Phys.* **450**, 110815.
- ZHU, G., CHEN, H., YAO, J. & SUN, S. 2019 Efficient energy-stable schemes for the hydrodynamics coupled phase-field model. *Appl. Math. Model.* **70**, 82–108.
- ZIMMERMANN, C., TOSHNIWAL, D., LANDIS, C.M., HUGHES, T.J.R., MANDADAPU, K.K. & SAUER, R.A. 2019 An isogeometric finite element formulation for phase transitions on deforming surfaces. *Comput. Meth. Appl. Mech. Engng* **351**, 441–477.